ANALYTICAL MODELING OF THE REPAIR OF IMPACT-DAMAGED PRESTRESSED CONCRETE BRIDGE GIRDERS

Michael Joseph Gangi

Thesis submitted to the faculty of the
Virginia Polytechnic Institute and State University
in partial fulfillment of the requirements for the degree of

Master of Science
In
Civil Engineering

Ioannis Koutromanos, Chair

Carin L. Roberts-Wollmann Thomas E. Cousins

June 5, 2015
Blacksburg, Virginia

Keywords: Bridge Repair, Analytical Modeling, FEM, FRP, FRCM, Splices

ANALYTICAL MODELING OF THE REPAIR OF IMPACT-DAMAGED PRESTRESSED CONCRETE BRIDGE GIRDERS

Michael Joseph Gangi

ABSTRACT

Highway bridges in the United States are frequently damaged by overheight vehicle collisions. The increasing number of prestressed concrete bridges indicates that the probability of such bridges being impacted by overheight vehicles has increased. This thesis, sponsored by the Virginia Center for Transportation Innovation and Research (VCTIR), investigated three repair techniques for impact damaged prestressed bridge girders: strand splices, fiber reinforced polymer (FRP) overlays, and fabric reinforced cementitious matrix (FRCM) overlays. The flexural strength of four AASHTO Type III girders, three of which were intentionally damaged and repaired, was evaluated. Six experimental tests were performed on these girders: one undamaged girder test and five repair method tests.

Nonlinear beam models and three-dimensional finite element (FE) models were created to predict the behavior of the beams under flexural testing, and subsequently validated and calibrated to experimental test data. The very good accuracy of the beam models indicated that they can be used alone for the performance assessment of damaged and repaired girders. Of course, the analyst must always be aware of the fact that a beam model cannot explicitly account for potentially crucial effects such as diagonal cracking. A direct comparison between repair methods was made by creating analytical models of a prototype girder setup. FRP overlays were seen to restore the most strength, while strand splices were seen to restore the most ductility. From observation, combining repair methods resulted in an additive effect on strength, but the deformation at onset of failure will be governed by the less ductile method.

ACKNOWLEDGEMENTS

I would like to express my sincere gratitude to Dr. Ioannis Koutroamnos for inviting me to partake in this research project and for guiding my efforts throughout this endeavor. He has made several contributions to this research, and his assistance in reviewing this document is very much appreciated. I would also like to thank my committee members Dr. Tommy Cousins and Dr. Carin Roberts-Wollmann, for their guidance and help throughout this research effort. It has been a pleasure working for all of you, and I thank you for your experience, guidance, and patience.

I would also like to thank my colleagues in this research project, Mark Jones and Justin Leisen. Without your work out in the lab with experimental testing, my analytical modeling would not be possible. It has been a pleasure working alongside of you, and I hope that you have enjoyed it as much as I have.

The hard work of Dr. Dave Mokarem, Brett Farmer, Dennis Huffman, Vanessa Pino, Bohan Bao, and Jiaxing Zhou is much appreciated. Without the effort of everyone contributing to this project, this research would never have taken place.

I would like to thank my family for their support and encouragement throughout my education. I would not be who I am today without you. Thanks to all of my friends I have made and kept throughout this endeavor, for having a sense of humor and being there when I needed a break.

Financial support was provided by both the Virginia Department of Transportation and the Federal Highway Administration.

All photos by Mark Jones, 2015.

TABLE OF CONTENTS

LIST OF FIGURES

LIST OF TABLES

ABBREVIATIONS

CFRP – Carbon Fiber Reinforced Polymer

FRCM – Fabric Reinforced Cementitious Matrix

FRP – Fiber Reinforced Polymer

NCHRP – National Cooperative Highway Research Program

ksi – Kips per Square Inch

VDOT – Virginia Department of Transportation

AASHTO – American Association of State Highway and Transportation Officials

LFRD – Load Resistance Factor Design

ACI – American Concrete Institute

FE – Finite Element

CHAPTER 1 INTRODUCTION

1.1 Background

Highway bridges in the United States are frequently damaged by vehicular accidents. Automobiles collide into highway bridges 25 to 35 times per year and per state (ElSaftey, et al., 2014). There is a growing need to assess the impact of the damage on the bridge and to know when repairs are necessary. A recent study conducted by Agrawal et al. investigated the frequency of bridges being struck by over-height trucks (Agrawal, et al., 2013). The state of Virginia reported 41 bridges damaged from over-height vehicle impacts from 2005 to 2008. Figure 1.1 shows the responses of state Departments of Transportation regarding the seriousness of the bridge impact problem in each state; dark grey and light grey represent bridge impacts as major and minor problems, respectively. The majority of states admitted that the damage of bridges from impact is a major problem (Agrawal, et al., 2013).

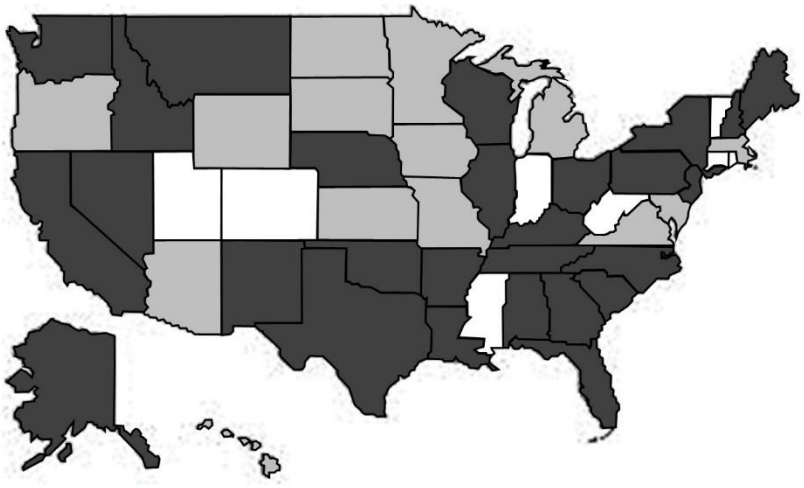

Figure 1.1: Over-height Impacts as Reported by State. Adapted from *Strikes on Low Clearance Bridges by Over-Height Trucks in New York State* by A. K. Agrawal, et al, 2013, Retrieved from http://www.rita.dot.gov/utc/publications/spotlight/2013_01/html/spotlight_0113.html. Copyright 2015 by U. S. Department of Transportation. Used under fair use, 2015.

The damage caused by vehicle impacts on bridges can range from minor to severe. Depending on the type of impact and volume of use of the bridge, these accidents can cause damage to property and even loss of life. The long-term economic impact can also be costly. Repairing or replacing damaged sections, diverting traffic, and hurting nearby businesses are all financial risks associated with bridge damage. In 1999, Iowa, Kentucky, Louisiana, and Mississippi reported an average cost of repair and/or cost of property damage of approximately $500,000 per damaged bridge (Fu, et al., 2003).

"Prestressing can be defined in general terms as the preloading of a structure, before application of the service loads, so as to improve its performance in specific ways" (Nilson, 1987). The application of a preload allows designers to offset the deflection, reduce materials required, increase the span lengths, and accelerate the construction timeline through the use of precast and segmental construction techniques. Because of these advantages, the popularity of using prestressing in the construction of bridges has increased.

Prestressed concrete bridges constitute more than 50% of all bridges in the United States. In addition, the Transportation Research Board Committee on Concrete Bridges assessed that the "application of prestressing to bridges has grown rapidly and steadily" (Aktan, et al., 1994). As research is conducted in making concrete lighter and stronger, the application of prestress to bridges extends the span capability of bridges of up to 800 ft for segmental concrete bridges (Aktan, et al., 1994). With the increasing number of prestressed concrete bridges in the United States, the probability of these bridges being impacted by overheight vehicles also increases.

The application of prestress on a bridge girder leads to a more complex problem when they are damaged, compared to if the girders were steel or reinforced concrete. Damage may cause strands to become exposed and susceptible to corrosion. It is important to accurately

assess and – if necessary – repair damaged members to restore the original resistance of the bridge. If the resistance cannot be restored, the bridge may be posted or replaced. Some of the current techniques used to repair prestressed bridge girders include strand splices, Fiber Reinforced Polymer (FRP), and Fabric Reinforced Cementitious Matrix (FRCM). Other techniques include steel jacketing, external post tensioning, and replacement (Kasan, 2009).

This thesis is intended to evaluate the efficiency of three repair methods. Through a review of previous applications and research of these repair techniques, the most promising three were included in a testing program. A series of experiments have been conducted on full-scale girders. The girders have been obtained from an Interstate-81 overpass near Arcadia, Virginia, which had been damaged by an over-height vehicle. Jones provides the bridge blueprints (Jones, 2015). Due to the damage from this and previous impacts, the Virginia Department of Transportation (VDOT) decided that the bridge would be replaced. The four AASHTO Type III prestressed girders, pictured in Figure 1.2, were provided to Virginia Tech to test repair techniques. Due to the removal procedure, the tested girders had deck sections that were approximately the width of the precast girder and were the thickness of the cast-in-place deck.

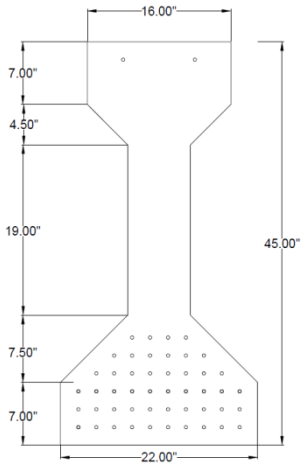

Figure 1.2: Typical AASHTO Type III Girder Cross Section Tested

1.2 Purpose and Scope

This VDOT sponsored thesis investigates repair techniques for impact damaged prestressed bridge girders. The investigation includes evaluation of the flexural strength of four AASHTO Type III girders, three of which were intentionally damaged and repaired. In addition, analytical modeling was used to aid in the development of design protocols for each repair method. This thesis discusses the creation of nonlinear beam models and three-dimensional finite element models to predict the behavior of the beams under flexural testing, and the extension of these models to investigate the effectiveness of these repair methods on a prototype girder with an effective bridge deck. Three Master of Science students collaborated on obtaining results: Justin Liesen, Mark Jones, and Michael Gangi. Leisen and Jones had responsibility for the testing of the repaired girders and Gangi performed the analytical modeling of the girders reported herein.

The objective of this thesis is to investigate the three repair methods tested: strand splices, Fabric Reinforced Polymer (FRP), and Fabric Reinforced Cementitious Matrix (FRCM). The investigation includes comparison of analytical models to test data as well as a determination of the effectiveness of the repairs in more realistic situations with the prototype girder a full width of deck.

1.3 Thesis Organization

The second chapter of this thesis reviews the literature associated with the design of prestressed concrete bridges, repair techniques for damaged prestressed bridges, and analytical modeling of these repair techniques. Chapter 3 discusses the six experimental tests performed on damaged and repaired girders. Chapter 4 describes the two types of analytical models developed

for the analysis of damaged and repaired girders, nonlinear beam models and three-dimensional, continuum-based finite element models. Chapter 5 discusses the validation of both the nonlinear beam models and the continuum-based FE models, comparing the tested and calculated data from the reported tests. Chapter 6 describes the use of analytical modeling to run tests on equivalent prototype girder test setups to make a direct comparison between repair methods. The direct comparison test chosen to be run is with AASHTO loading conditions and limit states. Chapter 7 provides conclusions and recommendations for future research. Appendices are included in Chapter 8.

CHAPTER 2 REVIEW OF LITERATURE

2.1 Introduction

As the majority of the investigation reported herein involves analytical modeling of a set of repaired impact-damaged bridge girders, it is important to first briefly explore the work which has already been conducted on this subject. This chapter consists of a review of previous research concerning analytical modeling of damaged and repaired bridge girders. It also includes the considerations of AASHTO bridge modeling and repair methods examined in this thesis.

2.2 AASHTO LRFD Requirements

Section 4.6.3 of the American Association of State Highway and Transportation Officials (AASHTO) LRFD Bridge Design Specifications provides the minimum requirements for using refined methods of analysis (AASHTO, 2010). First, consideration is given to aspect ratios of elements, positioning and number of nodes, and other topological features which might affect the accuracy of the solution. A structurally continuous railing, barrier, or median, acting compositely with the supporting components, may be considered to be structurally active at service and fatigue limit states.

In beam-slab bridges, the maximum acceptable aspect ratio of finite elements is 5.0. Sudden changes in either size or shape of finite elements should be avoided. The nodal loads need to be statically equivalent to the physical loads applied. At least five nodes per beam should be employed, though nine is preferable. For finite-element analyses which involve plate or beam elements, it is best to maintain the relative vertical distances between elements. If this is impractical, longitudinal and transverse elements may be placed at the midthickness of the plate-

bending elements if the eccentricities are accounted for in the equivalent properties of the composite sections (AASHTO, 2010).

For the deck, flexural and torsional deformation must be considered, but vertical shear deformation need not be. The wheel loads on the deck should be modeled as patch loads distributed over an area approximating the wheel contact surface. For the material properties of the deck elements, if a bridge deck is solid with uniform depth and the stiffness is approximately equal in every in-plane direction, it can be considered isotropic (AASHTO, 2010).

Inelastic behavior must be restricted to the flexure of beams or girders. Inelastic behavior resulting from shear and/or uncontrolled buckling is not allowed (AASHTO, 2010).

2.3 Design of Repair Techniques

In 1980, Shanafelt and Horn conducted research for The National Cooperative Highway Research Program (NCHRP). They investigated 11 different repair techniques including external post-tensioning, steel jacketing, strand splicing, combinations of these methods, and replacement. Their results were published in NCHRP Report 226 along with an initial damage classification system. The report suggested standards for inspection and repair of damaged prestressed bridge girders to include proper techniques, tools, and forms (Harries, et al., 2012). Subsequent research into repair techniques have built on and expanded the research reported in NCHRP Report 226.

Replacement is typically seen as the safest and surest way to handle a damaged girder. However, it is the most expensive and time consuming. According to a study conducted for the Washington Department of Transportation, most girder replacements cost between $500,000 and

$1,000,000 depending on the size and scope (average of around $8,000 per foot of girder replaced) and took approximately one to two months to complete the replacement (Brice, 2013).

Ultimately, any repair method, or combination of repair methods is going to be more cost and time effective than replacing a damaged girder. In addition, if designed appropriately, the repaired section may outperform the original design capacity of the girder. Strand splices, fiber reinforced polymer (FRP) and fabric reinforced cementitious matrix (FRCM) are investigated in this thesis.

2.3.1 Strand Splice

In the event that one or more strands are severed on a damaged prestressed girder, the severed ends can be reconnected using a strand splice or splice chuck. The re-connected strand can then be stressed to reintroduce some or all of the force that was initially in the strand using one of three methods. The bridge can be preloaded introducing a negative moment, or upward camber, and after the strands are connected and the load removed, tension is induced. Another option is to heat the strand to cause strand elongation before the splice is connected. Once the strand cools, it shrinks and tension is introduced. The final technique is to use a wrench to torque the strand splice chuck and induce tension. Because introducing a negative moment is not an option in most cases and strand heating may change the material properties of the strands, torqueing the turnbuckle on the splice chuck is the most common way to induce tension into the severed strands (Harries, et al., 2012).

Kasan et al. presented the modeling recommendations for strand splices (Kasan, et al., 2014). Strand splices cannot be universally relied on to develop the ultimate capacity of the strands or to fully restore the capacity of the elements in which they are used. It is recommended

that strand splices should be limited to strand diameters 0.5 in and less. They should also be limited to restoring in situ prestress forces less than $0.70f_{pu}$. They are limited to developing $0.85f_{pu}$, thereby reducing their effectiveness in restoring the ultimate capacity of strands. Strand splices should be staggered when placed, shown in Figure 2.1, and limited to splicing 15% of strands in a girder, regardless of staggering.

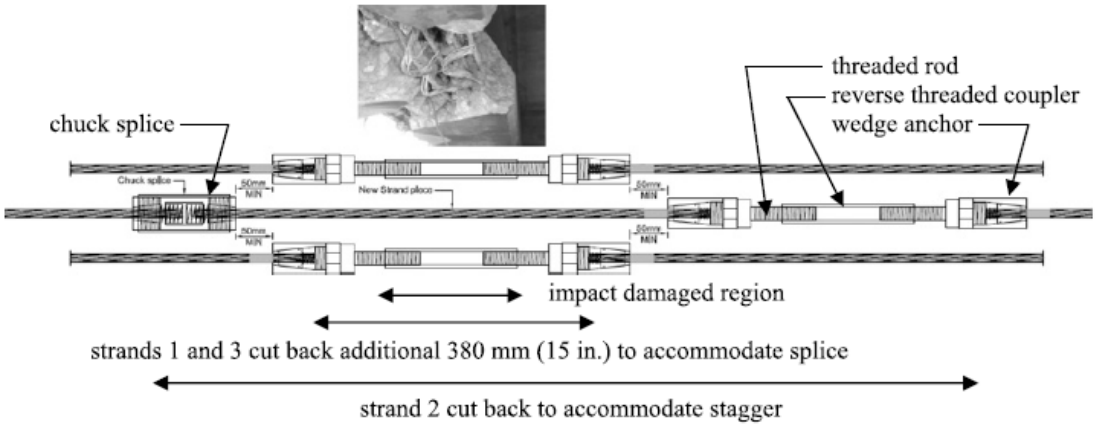

Figure 2.1: Strand Splice Staggering. Adapted from "Repair of Prestressed-Concrete Girders Combining Internal Strand Splicing and Externally Bonded CFRP Techniques," by J. L. Kasan, et al., 2014, *Journal of Bridge Engineering, 19*, p. 201. Copyright 2014 by ASCE. Used under fair use, 2015.

Strand splices are one of the cheapest and easiest to design and install methods for repairing damaged prestressed girders. They can restore most of the strength and some of the force lost due to the damage. The size and stiffness of the splice must be considered to ensure that proper positioning and cover are given and to account for any unintended eccentricities. In addition, the advertised minimum strength of a strand splice is 85% of the nominal strength of the strands it is joining. This must be considered as it will create a potential critical failure point (Kasan, 2009).

2.3.2 Fiber Reinforced Polymer (FRP)

Fiber reinforced polymer (FRP) is a polymer matrix impregnating high performance fibers. The fibers can be made from aramid, carbon, glass, high performance steel, or a hybrid of these materials (Harries, et al., 2012). Carbon fiber reinforced polymer (CFRP) laid as a unidirectional fabric is one of the most common forms of FRP and is supplied in large rolls of fabric. The CFRP system is composed of primer, putty, saturant, carbon fiber sheets, and a protective topcoat (Wipf, et al., 2004b). CFRP has a tensile capacity about 1.5 times prestressing strands and a Young's modulus of 75% of that of steel (Harries, et al., 2012). This is evident in the stress-strain relationship for carbon fiber shown in Figure 2.2 (Wipf, et al., 2004b). These properties allow carbon fiber to reach a much higher strain than steel, but it does not have the plastic behavior or strain hardening characteristics associated with steel (Harries, et al., 2012)..

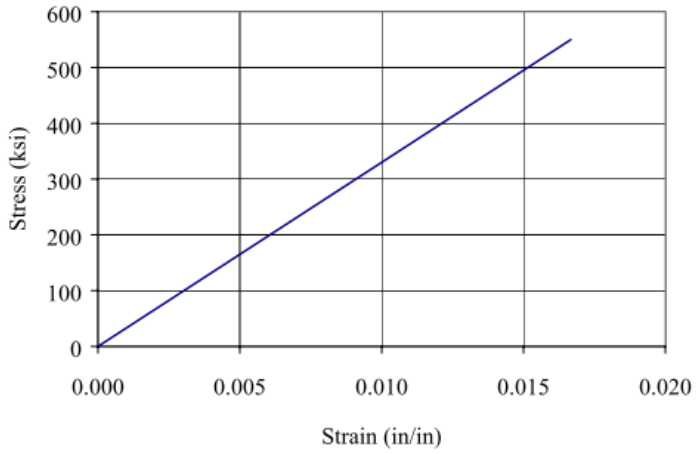

Figure 2.2: Carbon Fiber Stress Strain Curve. Adapted from "Repair of Impact Damaged Prestressed Concrete Beams with CFRP," by T. J. Wipf et al., 2004, *Effective Structural Concrete Repair, 1,* p. 82.

ACI Committee 440 provides the modeling recommendations for externally bonded FRP repair systems (ACI , 2008). For the calculation of the flexural strengthening effect of adding

longitudinal FRP reinforcement, many assumptions are made. Assumptions include: there is no relative slip between external FRP reinforcement and concrete, the shear deformation within the adhesive layer is neglected because the adhesive layer is very thin with slight variation in thickness, and the FRP reinforcement has a linear elastic stress-strain relationship to failure. It is important to determine the strain level in the FRP reinforcement at the ultimate limit state. Because FRP materials are linear elastic until failure, the level of strain in the FRP dictates the level of stress developed in the FRP. The maximum strain level that can be achieved in the FRP will be governed by either the strain level developed in the FRP at the point at which the concrete crushes, the point at which the FRP ruptures, or at the point at which the FRP debonds from the substrate (ACI , 2008).

Fiber reinforced polymers provide a wide array of options for repair, but the designer must consider the unique material properties of the different types of fabrics along with the specific repair method they choose. In addition, the installation process requires skilled laborers and the adhesive used to bond the system to the girder must be protected from the environment to prevent deterioration from ultraviolet rays and fire (Kasan, 2009).

2.3.3 Fabric Reinforced Cementitious Matrix (FRCM)

FRCM is comprised of a cementitious matrix and a fiber grid. The matrix is impregnated through the mesh to form a bond between the fabric strands and the girder. The grid geometry of FRCM gives it advantages when compared to FRP. One of the advantages to a grid geometry is bi-axial strength. This bi-axial strength allows for the system to provide shear resistance without requiring additional layers in the transverse direction as required by FRP. By reducing the amount of material and the number of applications, the FRCM will also reduce the risk of

overdesign due to the necessity of additional layers to resist secondary stresses. The designer, however, must be aware of the potential to over design FRCM similar to FRP. Installation of FRCM requires skilled laborers and the temperature during installation must be managed as much as possible to ensure that it does not affect long term performance (ACI, 2013).

ACI Committee 549 provides the modeling recommendations for the externally bonded FRCM repair (ACI, 2013). The FRCM composite material bonded to the surfaces of members may be used to enhance the design flexural strength of sections by acting as external tension reinforcement. In such cases, sectional analysis is based on many assumptions. Assumptions include the bond between the FRCM and the substrate remaining effective, and the FRCM having a bilinear behavior to failure in which only the second part of the curve used in design and analysis. The flexural strength of a section depends on the controlling failure mode. Effective tensile strain level in the FRCM reinforcement attained at failure should be limited to the design tensile strain of the FRCM composite material (ACI, 2013).

Fabric-Reinforced Cementitious Matrix (FRCM) has a primary and secondary orientation which allows it to provide bi-axial tensile strength and gives it some shear resistance. However, the installation procedure requires a specified temperature range and a specialized professional. Since it is relatively new in comparison to some of the other techniques, finding someone with installation experience may prove difficult. In addition, there is a longer cure process for the cementitious matrix than epoxy. If the matrix is not given the proper cure time or temperatures are not within range, a good bond between the fabric and the substrate may not form. Without a proper bond, the repair will not function properly (ACI, 2013).

2.4 Analytical Modeling of Bridge Repairs

Zou and Luo presented a report on finite element analysis of damage to a prestressed concrete girder, specifically corrosion damage (Zou & Luo, 2012). A three-dimensional nonlinear finite element model was created of a representative test girder in ANSYS. The concrete was modeled by SOLID65 solid elements, supports were modeled by SOLID45 solid elements, and steel bars were modeled by LINK8 beam elements. Because of the symmetry of the structure, only half of the girder was modeled. The properties of the steel strands were changed to show the effects of the corrosion. A displacement-controlled analysis was run to failure. The results concluded that when the corrosion rate is less than 5%, the girder shows a steel yielding failure and is tension controlled. However, when corrosion rate is relatively more than 5%, the failure is a compression controlled concrete crushing (Zou & Luo, 2012). This study was not backed by experimental testing.

Sen et al. used nonlinear finite element modeling to verify the results of experimental testing on repaired bridge sections (Sen, et al., 2001). Six test specimens were used in the study, each a concrete/steel composite bridge model with an effective concrete deck and a steel girder. Varying levels of damage were simulated in the study by pre-loading the specimen past yield of the tension flange, causing permanent deformation. Beams were then repaired with carbon fiber reinforced polymer (CFRP) epoxy laminates. The nonlinear finite element analysis program PCFRAME was used to predict the response of the six steel composite bridge sections tested. A fiber-section approach was used in modeling the test using nonlinear beam analysis. The concrete slab was discretized into 20 layers, the steel reinforcement by two, the wide flange section as eight steel layers, and the CFRP laminate and adhesive as single layers. Agreement

for the load-deflection was not close with the finite element analysis predicting a stiffer post-yield response. This was because the effect of pre-damage was only approximated in the analysis. The overall agreement between experiment and finite element analysis was satisfactory (Sen, et al., 2001).

Kim et al. used a full-scale finite element analysis to investigate the behavior of a four-span prestressed concrete girder bridge damaged by impact loads and repaired (Kim, et al., 2008). The Main Street Bridge, located in Winnipeg, Manitoba, Canada, was constructed in 1963. The exterior bridge girder was frequently struck by heavy trucks. The impact loads caused spalling of the concrete and complete rupture of the steel strands. A repair was designed and implemented using prestressed CFRP sheets. The CFRP was designed to restore strength to meet demand of the AASHTO HSS 25 design truck. To investigate the effectiveness of the site application and corresponding flexural behavior of the repaired bridge girder, a three-dimensional finite element analysis was performed in ANSYS. Four-node elastic shell elements (SHELL 63) and 3D spar elements (LINK 8) were used for the concrete and the prestressing strands, respectively. The unidirectional prestressed CFRP sheets were simplified to 3D spar elements. The prestressing was applied to the model by including initial strains in the spar elements. To investigate the effect of the repair, the bridge models included three different states: undamaged, damaged, and repaired. The design trucks were located to induce the maximum moment in the girders (Kim, et al., 2008). The study used a linear elastic model that may not accurately predict the behavior of the bridge since cracking is not included. It also did not back up the models with experimental testing.

Shapiro used a full-scale finite element model to investigate the behavior of a damaged two-span bridge and predict the effectiveness of a repair (Shapiro, 2007). In 1992, large and

unexpected cracks were discovered in prestressed concrete girders of several recently-constructed bridge spans of I-565 in Huntsville, Alabama. The cracking was not determined to be of immediate concern, but a repair using externally bonded, fiber-reinforced polymer (FRP) reinforcement was proposed. Testing was done on a pre-repair segment of the bridge. A finite element model was created in ABAQUS/CAE and was refined by the pre-repair test data. Concrete elements were modeled using 8-node linear brick C3D8R elements that incorporate reduced integration and hourglass control. Shell elements were used for steel reinforcement, the load application, and the FRP (Shapiro, 2007). The model of the post-repair bridge was used to predict changes in behavior that should occur when the repair is installed, yet tests were not conducted to verify the post-repair behavior.

Kasan used finite element modeling to investigate the effectiveness of a series of repair methods on a wide-range of prototype prestressed concrete bridge girder shapes (Kasan, 2009). The repair methods investigated were CFRP strip, CFRP fabric, near-surface mounted (NSM) CFRP, Prestressed CFRP, post-tensioned CFRP, and post-tensioned steel. The three prototype prestressed concrete girder shapes investigated were adjacent boxes, spread boxes, and AASHTO type I girders. Biaxial nonlinear fiber element sectional analysis was done in the program XTRACT. This program can perform moment-curvature sectional analysis. Bridge loading was calculated based on the HS-25 design truck, and compared to loading applied by the HS-20 design truck that was used in 1960 when many highway bridges were designed (Kasan, 2009). There are limits to the sectional models created because they do not account for full beam bending behavior. The models also were not verified to experimental testing of the girder sections.

CHAPTER 3 EXPERIMENTAL TESTS ON DAMAGED AND REPAIRED GIRDERS

3.1 Experimental Tests on Damaged and Repaired Girders

Previous studies have investigated the structural repair of prestressed concrete bridge girders. In 2007, Shapiro developed a finite element model of an in service bridge repaired using FRP to verify the behavior of the system both pre- and post-repair (Shapiro, 2007). In 2009, Kasan investigated the general repair of prestressed concrete bridge girders with different repair techniques and developed analytical models to determine the repair effectiveness (Kasan, 2009). These previous studies either did not investigate a broad enough range of repair methods or did not verify the analytical modeling of the repair methods with experimental testing. Given the limited research in this area, this thesis aims to investigate the specific damage scenario of impact damage on a prestressed concrete girder. It also provides a comprehensive review of repair methods using analytical models that are verified with experimental testing.

During this investigation, six flexural tests were conducted on four standard AASHTO Type III girders. Flexural tests were seen to be representative of the strength of the damaged, repaired regions because typical impact damage from overheight vehicles occurs around the mid-span of a girder. In these mid-span regions, due to the type of loading on the simple span, flexural strength is often of concern, and shear strength is usually sufficient. Shear strength was checked for every girder using AASHTO calculations to ensure this assumption was valid.

Figure 3.1 shows the cross-section of the typical AASHTO Type III girder being investigated in all tests, with the remaining deck provided after its removal from service. Each girder has 50 Grade 250 low relaxation prestressing strands with a nominal diameter of 3/8 in, as

shown in the bridge blueprints (Jones, 2015). Eight of the 50 strands are harped strands, meaning that at the ends of the beam these strands are located near the top of the cross-section, and at the center of the beam they are located near the bottom of the cross-section. The harping points on the 60 ft girders are located 24 ft from each girder end. The result is a strand eccentricity that varies linearly from supports to the harping points, and is constant throughout the 12 ft midspan region. This is commonly done in prestressed concrete beams because at initial transfer of prestressing forces, the stresses at the end of the beam can often control the design if the eccentricity of strands near the supports is too high. The average deck was assumed to be 16 in, which is the width of the top flange of the girder. An average was taken because width varied along the length of each girder. The deck varied from 15 in to 24 in, so an average of 16 in deck was assumed. The thickness of the deck, measured to be 9.5 in, was assumed to be 8.75 in to account for the presence of 0.75 in indentations in the top of the deck created during removal by saw cutting.

The first test was a flexural test of an unrepaired 44 ft-long section to establish a baseline for comparison with the subsequent tests. The second test was a flexural test on a 60 ft girder that was damaged and repaired at the midpoint (30 ft) using the strand splice method. The third and fourth tests were flexural tests on the same 60 ft girder, which was damaged and repaired at two distinct points, with each damaged area located 20 ft from the end of the girder. Both tests were completed on the same girder to maximize the number of tests conducted with the finite number of specimens. The two repair techniques evaluated in Tests 3 and 4 were strand splice and Fiber Reinforced Polymer (FRP), respectively. The fifth and sixth tests were flexural tests on the same 60 ft girder, which was damaged and repaired at in the same locations as the girder tested in Tests 3 and 4. The two repair techniques evaluated in Tests 5 and 6 were Fabric

Reinforced Cementitious Matrix (FRCM) and the combination of FRCM and strand splices, respectively. Table 3.1 delineates the testing schedule for this project and summarizes the setup and test results. Figure 3.2, Figure 3.3, Figure 3.4, Figure 3.5, Figure 3.6, and Figure 3.7 show the test layouts for each test.

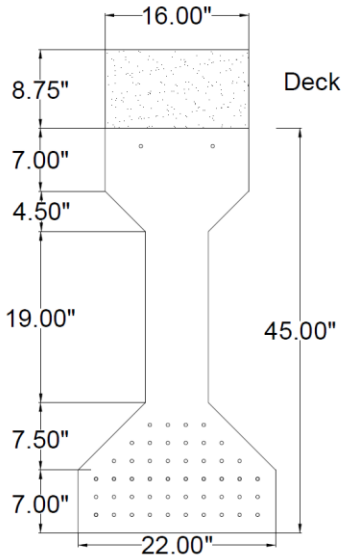

Figure 3.1: Girder Cross-Section

Table 3.1: Testing Schedule and Summary

Tested Repair	Number of Severed Strands	Repair Investigated	Span Length (ft)
Control Test	N.A.	N.A.	35
8-Strand Splice	8	Strand Splice	58
4-Strand FRP	4	FRP	48
			53
4-Strand Splice	4	Strand Splice	58
			50
4-Strand FRCM	4	FRCM	52
4-Strand Splice and FRCM	4	Strand Splice & FRCM	52

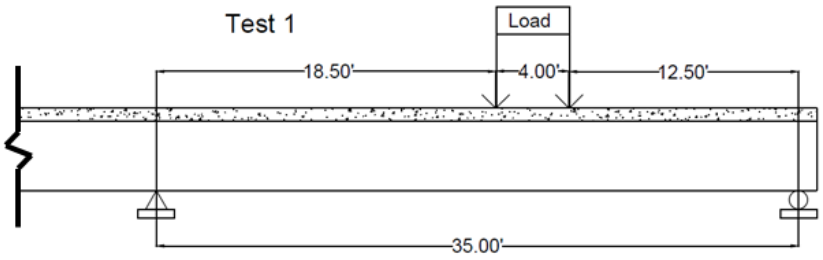

Figure 3.2: Test 1 Setup

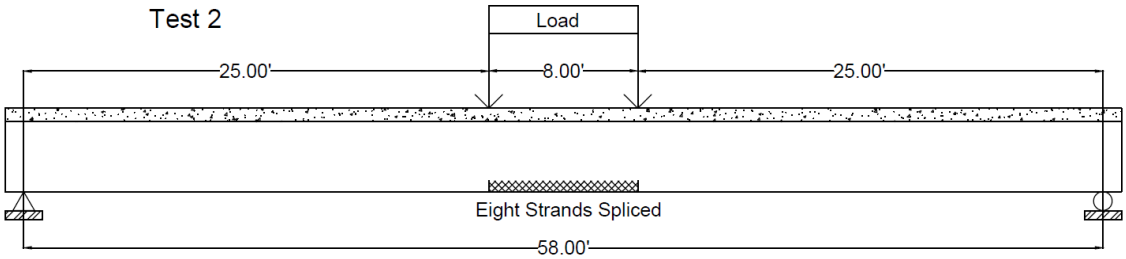

Figure 3.3: Test 2 Setup

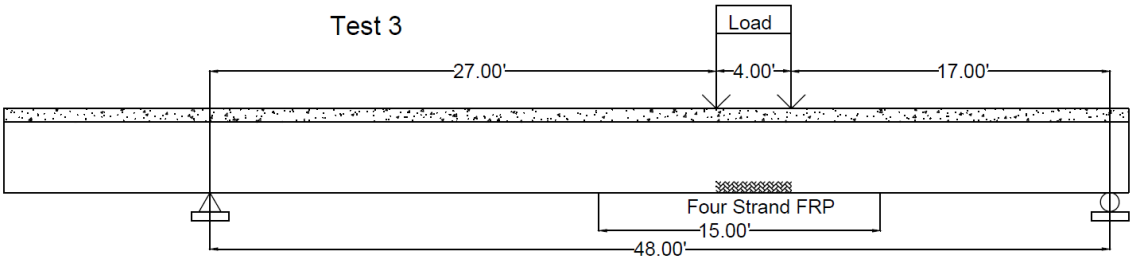

Figure 3.4: Test 3 Setup

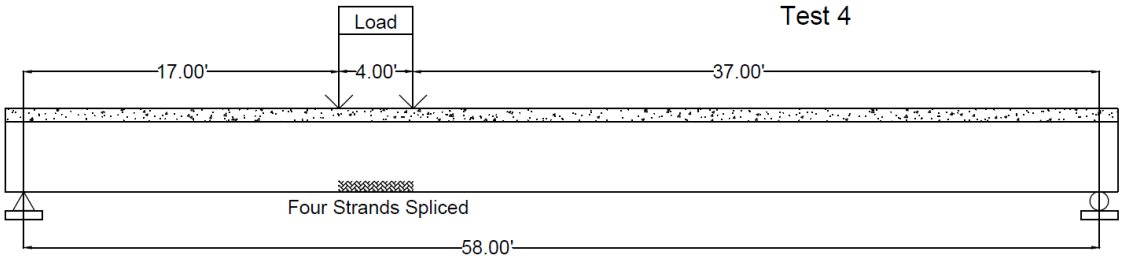

Figure 3.5: Test 4 Setup

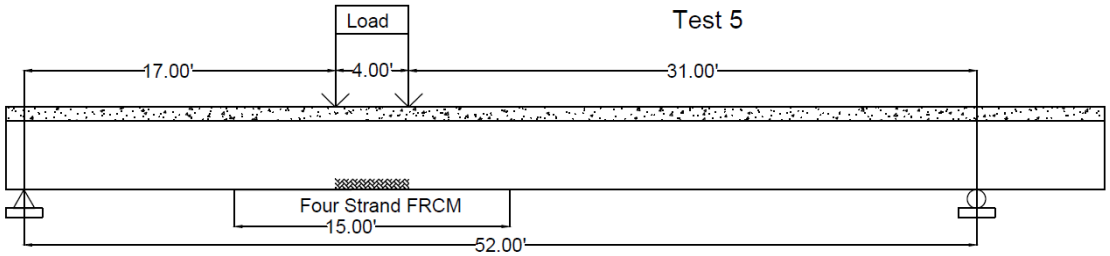

Figure 3.6: Test 5 Setup

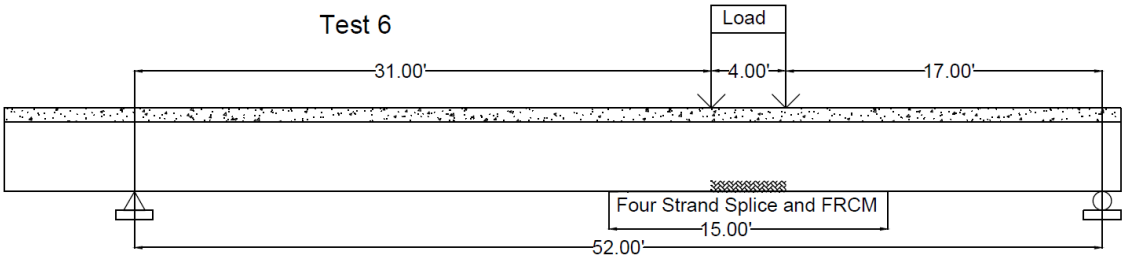

Figure 3.7: Test 6 Setup

The girder used in the first test had been damaged due to vehicle impact. The remaining three girders were intentionally damaged at specific locations by the lab personnel to reproduce the anticipated effect of impact by an over-height vehicle. The concrete in these regions was removed using a hydraulic hammer and the prestressing strands were severed.

The girder used in Test 2 had eight strands severed and repaired with strand splices. The girder used for Tests 3 and 4 had two separate damage and repaired sections. An FRP repair was done on the right side of this girder on four severed strands and used in Test 3. On the left side of the girder, four strands were severed and repaired and used in Test 4. The girder used for Tests 5 and 6 also had two separate damage and repaired sections. An FRCM repair was done on the left side of this girder on four severed strands and used in Test 5. On the right side of this girder, four strands were severed and repaired with a combination of strand splices and FRCM

and used in Test 6. Once the repairs were complete, flexural tests of the girders were conducted to determine the effective strength of the repair method.

3.2 Test 1 - Control Test

The girder used in Test 1 sustained damage during removal and transportation from the bridge site to the laboratory. As a result, shear cracking occurred causing a 16 ft portion of the girder to separate from Girder A. This portion was later used to gather samples of concrete, reinforcing bar, and strand materials for testing. The remaining 44 ft portion of the girder was used as a control to gather the undamaged and unrepaired properties of girder section being investigated. The left support was placed in a region that would normally be the midspan of the girder, and have minimal shear reinforcement. Minimizing the potential for shear failure was considered in the test set-up. Supports were placed to create a 35 ft simple span and the two point loads were offset 3 ft toward the right support, as shown in Figure 3.2. Test 1 was a flexural test of a 35 ft simple span length. The section was supported on two W21x101 steel sections with transverse stiffeners as supports. A pin bearing was placed on one steel section and a roller bearing was placed on the other. The girder was placed on top of the pin and roller bearings. A frame was used to hold a 400 ton hydraulic actuator above the load points. The actuator exerted a force on a 6 ft long steel spreader beam resting on two neoprene and steel laminate bearings that translated the load into a constant moment region between two load points. Figure 3.8 shows the loading system setup with the actuator, spreader beam, load frame, and laminate bearings.

.

Figure 3.8: Test 1 Loading System

Data was continuously recorded using a high speed data acquisition system. Figure 3.9 shows the instrumentation layout along the length of the girder. For the purposes of modeling the test results, the most important data acquired was the load applied and displacement at the center of the beam. Potentiometers were attached to the bottom of the girder to measure vertical deflection during the test. A 400 kip load cell was placed between the actuator and the load frame to measure the applied load.

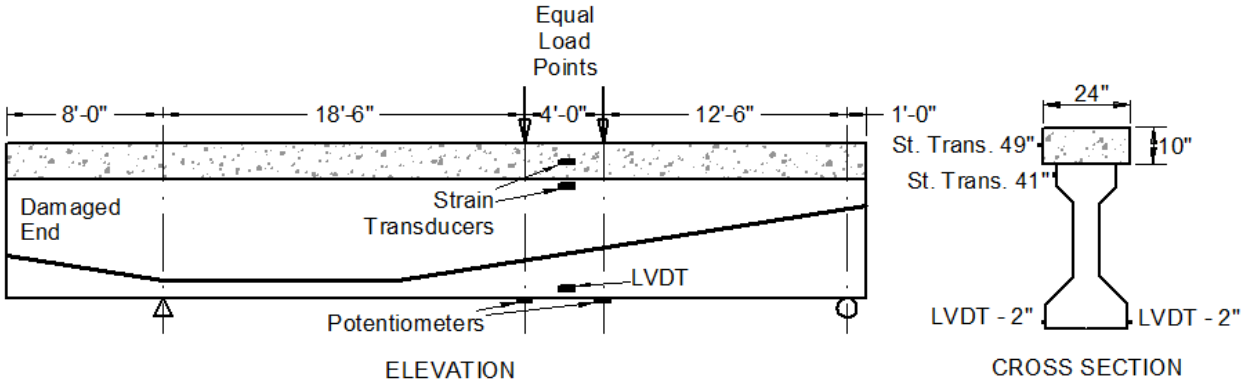

Figure 3.9: Test 1 Setup and Instrumentation

The girder was tested on May 27, 2014 to a load level of 353 kips. Initially, the rate of loading was managed to ensure there were no effects from sudden or impact loading. The load was applied in approximately 20 kip increments. At each increment, the girder was allowed to settle and cracks were inspected, highlighted, and marked. The test was stopped at a load level of 353 kips due to malfunction of the hydraulic pump used for the load application on the beams. The pump was replaced and testing resumed on June 2, 2014. During this second attempt, the girder was re-loaded up to a load level of 401 kips, corresponding to the capacity of the test frame. Thus, since capacity was reached, testing stopped at this point. Inspection of the specimen after the test led to the observation that multiple flexural cracks, as shown in Figure 3.10, and to the conclusion that flexural failure was imminent.

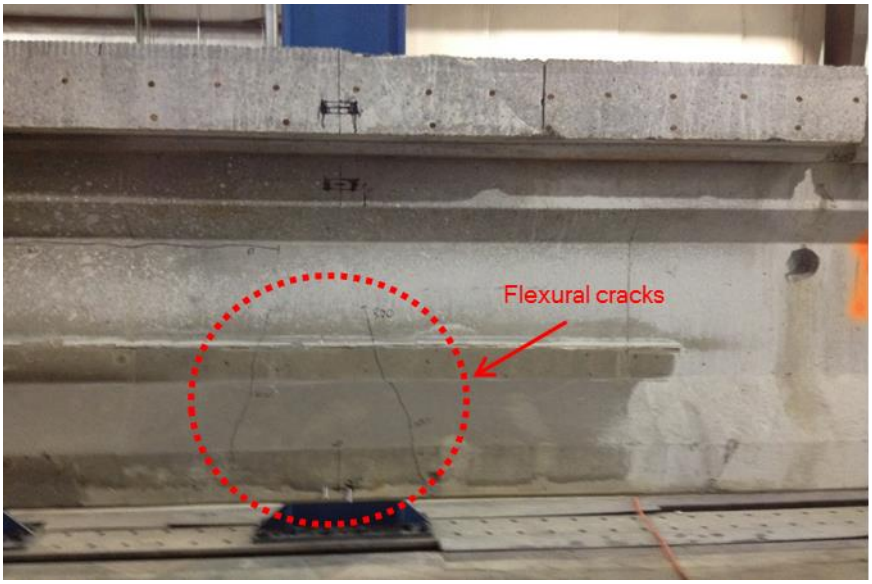

Figure 3.10: Flexural cracks in Test 1 Beam

3.3 Test 2 - Girder with Eight Severed/Re-tensioned Strands

The girder used in Test 2 was damaged 4 ft on either side of the midpoint. Of the 48 prestressing strands in the bottom flange of the girder, eight were intentionally severed during damaging. The location of the damage is shown in Figure 3.11. The locations of the strands that were severed are shown in Figure 3.12. The length for the damage on this girder was chosen to be 8 ft based on data from the YRC Freight Company indicating the average width of a semi-trailer as approximately 8 ft (YRC Worldwide, 2015). Eight strands, or 16% of the strands, were chosen to be severed based on a poll of State Departments of Transportation conducted in 2004 (Wipf, et al., 2004a). Some Departments of Transportation reported that a prestressed girder is replaced if any strand is damaged from the impact of over-height vehicles. Other Departments of Transportation reported that a prestressed girder is replaced when 10% of strands were damaged. The maximum number of damaged prestress strands allowed to be repaired by any state before the damaged girder would be replaced was 25% (Wipf, et al., 2004a).

Considering this data, damaging 16% of strands would provide a test of a damaged girder in a controlled setting. The damage would be greater than that which is consistently allowed by Departments of Transportation before it would be considered too damaged to repair. Subsequently damaged test girders were inflicted with less damage and the data from all tests was scaled to compare results. In addition, eight damaged strands on an AASHTO Type III girder is the maximum number of strands to efficiently repair using externally bonded FRP (Harries, et al., 2012).

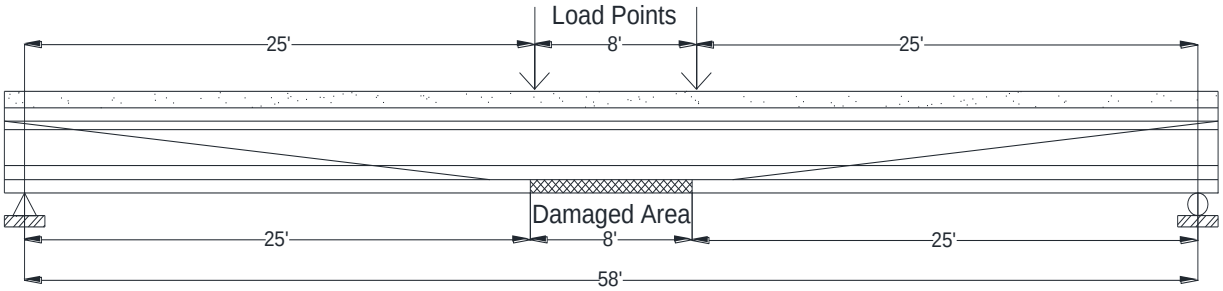

Figure 3.11: Test 2 Damage Location

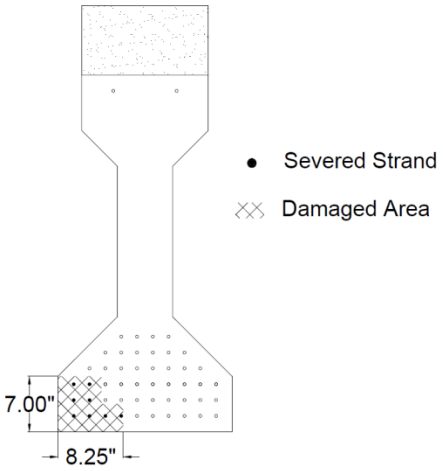

Figure 3.12: Test 2 Cross-Section through Damaged Area with Severed Strand Locations Shown

Test 2 was a flexural test of a 58 ft simple span length. Figure 3.13 is a picture along the length of the beam showing an overview of the setup. Data was continuously recorded using a high speed data acquisition system. Figure 3.14 shows the instrumentation layout. For the purposes of modeling the test results, the most important data acquired was the load applied and displacement at the center of the beam. Three potentiometers were attached to the bottom of the girder to measure vertical deflection during the test. A 400 kip load cell was placed between the actuator and the load frame to measure the applied load.

Figure 3.13: Test 2 Setup

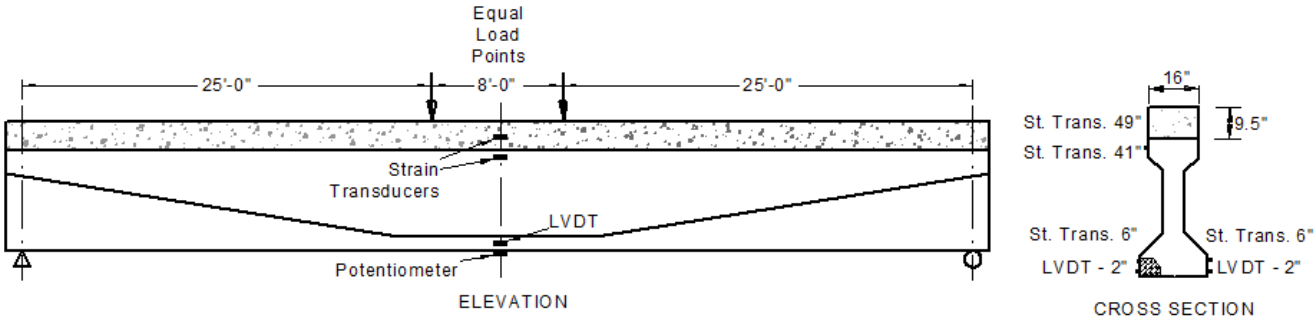

Figure 3.14: Test 2 Setup and Instrumentation

The girder was tested on August 21, 2014. Initially, the rate of loading was managed to ensure there were no effects from sudden or impact loading. The load was applied in approximately 40 kip increments. At each increment, the girder was allowed to settle and cracks were inspected, highlighted, and marked. The test was stopped at a load level of 195 kips and 3.39 in of deflection when one of the prestressing strands failed. Inspection of the specimen after the test revealed that two of the strand splices ruptured at the final load step and led to the conclusion that full flexural failure was reached. The flexural cracking pattern in the repaired section is shown in Figure 3.15.

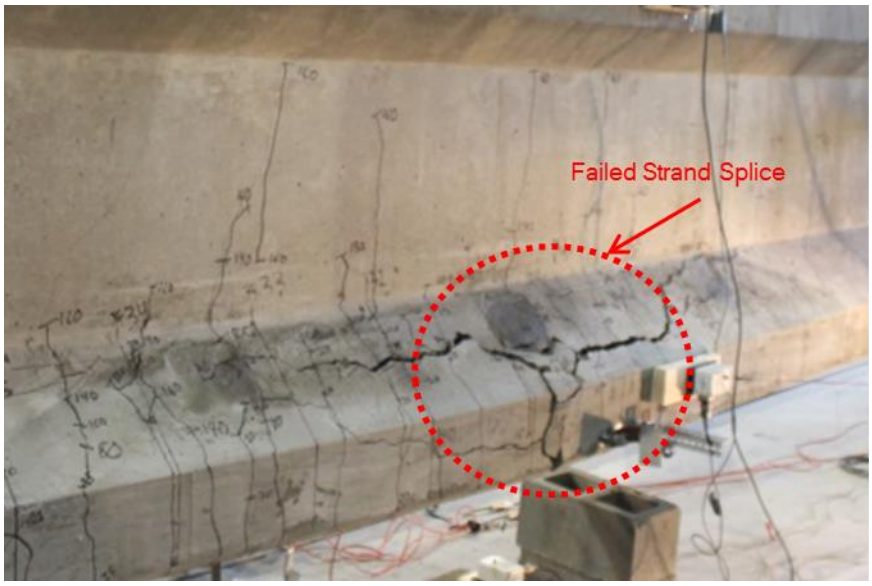

Figure 3.15: Failed Strand Splice in Test 2

3.4 Test 3 – FRP Repaired Girder with Four Severed Strands

The girder used in both Tests 3 and 4 was damaged in two separate regions. To space damage equally, the damage was centered at approximately the one-third and two-thirds points along the length of the girder. The length of this girder's damage was chosen to be 4 ft in two locations as shown in Figure 3.16. The two damage locations allowed two repair techniques to be tested on the same girder without one repair influencing the other repair's test results. In addition to reducing the length of damage, the number of severed prestressing strands was reduced to four strands. Figure 3.17 shows the locations of the strands that were severed during the damaging process.

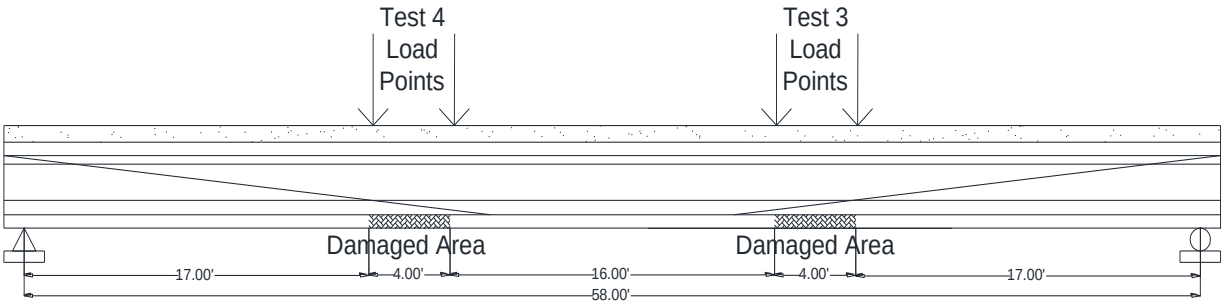

Figure 3.16: Tests 3 and 4 Girder Damage Locations

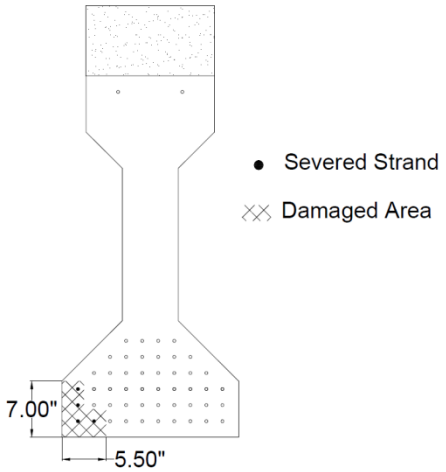

Figure 3.17: Tests 3 and 4 Cross-Section through Damaged Area with Severed Strand Locations Shown

A professional subcontractor conducted the repair for Test 3 with a high strength, quick set concrete patch and V-Wrap C400H FRP composite. V-Wrap C400H FRP is a 0.08 in thick fabric with V-Wrap 770 ambient cure epoxy resin provided by Structural Technologies (International Code Council Evaluation Service, 2014). After the concrete patch was placed and allowed to cure, the FRP was installed. Test 3 was a flexural test of a 48 ft simple span length for the first iteration and a 53 ft simple span length for the second iteration. The setup for Test 3, iteration 1 is shown in Figure 3.18. Data was continuously recorded using a high speed data acquisition system. Figure 3.19 and Figure 3.20 show the instrumentation layout along the length of the girder for the two iterations of Test 3. Three potentiometers were attached to the

bottom of the girder to measure vertical deflection during the test. A 400 kip load cell was placed between the actuator and the load frame to measure the applied load.

Figure 3.18: Test 3 Setup

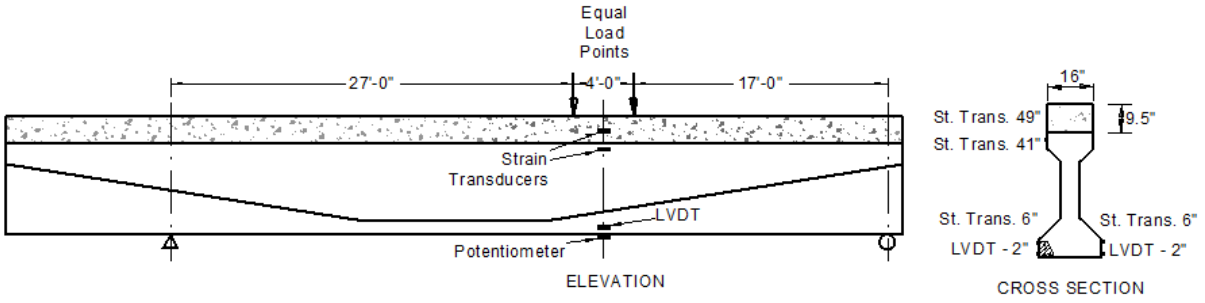

Figure 3.19: Test 3.1 Setup and Instrumentation

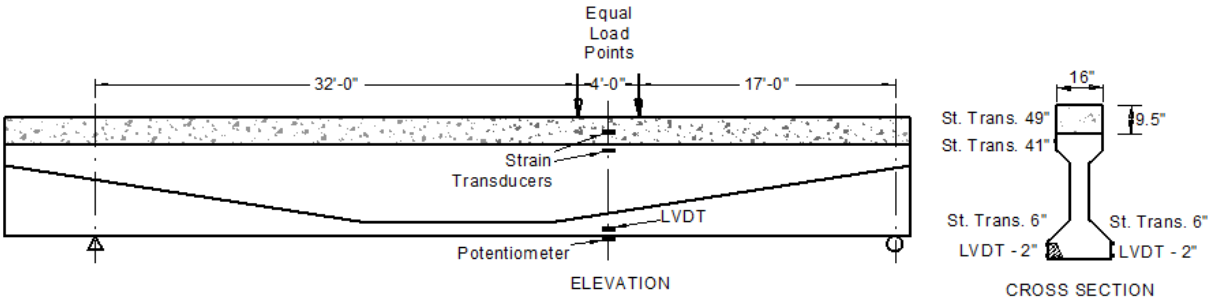

Figure 3.20: Test 3. 2 Setup and Instrumentation

The girder was tested on October 21, 2014. Initially, the rate of loading was managed to ensure there were no effects from sudden or impact loading. The load was applied at approximately 20 kip increments. At each increment, the girder was allowed to settle and cracks were inspected, highlighted, and marked. The test was stopped at a load level of 312 kips and 3.16 in of deflection due to the flexural cracking approaching the four strand splice repair section to be tested in Test 4. Inspection of the specimen after the test led to the observation that shear cracks in the web of the girder started to form in locations with minimal shear reinforcement as shown in Figure 3.21. The conclusion was to stop testing in order to avoid damaging the four strand splice repair section, propagating shear cracking, and adversely affecting the results of Test 4, though flexural failure was not imminent. Figure 3.22 shows the cracking observed at the load point near the peak load prior to stopping the test. The iteration of Test 3 was conducted on December 18, 2014. The test was stopped at a load level of 180 kips due to the actuator slipping and no longer exerting a consistent vertical force. Due to the lack of new information gleaned from this iteration, results from Test 3, iteration 2 are not included in this thesis.

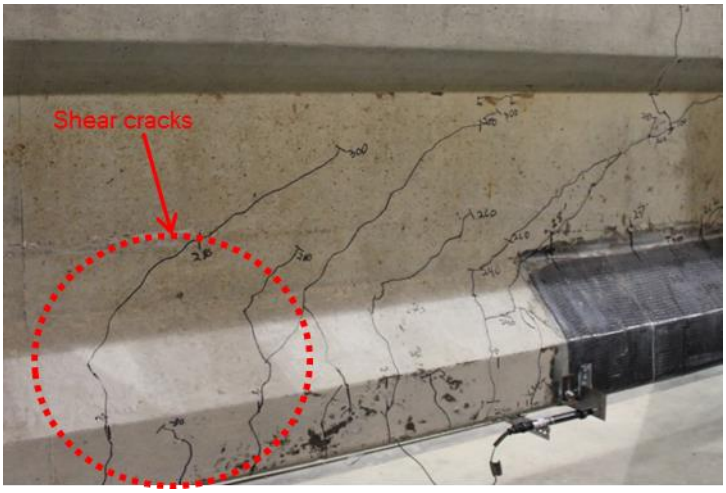

Figure 3.21: Test 3.1 Shear Cracking in Midspan Region

Figure 3.22: Test 3.1 Cracking Near Peak Load

3.5 Test 4 – Girder with Four Severed/Re-tensioned Strands

For Test 4, the same girder was used again, with the other four damaged strands being tested. The length for damage to allow this same girder to be damaged in two locations was chosen to be 4 ft as shown in Figure 3.16. The location of the four severed prestressing strands is shown in Figure 3.17. Two iterations of Test 4 were conducted. During the first iteration, the actuator slipped longitudinally in relation to the girder. For the second iteration, the span length was decreased to reduce the rotation of the beam at the load point and reduce the potential of the actuator slipping. A professional subcontractor conducted the repair of the four severed strands for Test 4 with strand splices. After the strands were spliced, they were encased in a high strength, quick set concrete.

Test 4 was a flexural test conducted in two iterations with a 58 ft simple span length for the first iteration and a 50 ft simple span length for the second iteration. The span length was decreased from 58 ft to 50 ft for the second iteration by moving the roller bearing 8 ft closer to the pin. Data was continuously recorded using a high speed data acquisition system. Figure 3.23 shows the instrumentation layout for the first iteration. Figure 3.24 shows the instrumentation layout for the second iteration. Three potentiometers were attached to the bottom of the girder to measure vertical deflection during the test. A 400 kip load cell was placed between the actuator and the load frame to measure the applied load.

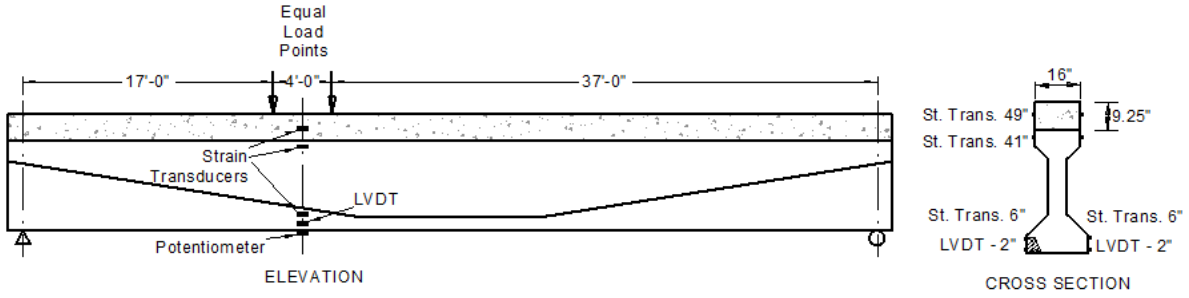

Figure 3.23: Test 4.1 Setup and Instrumentation

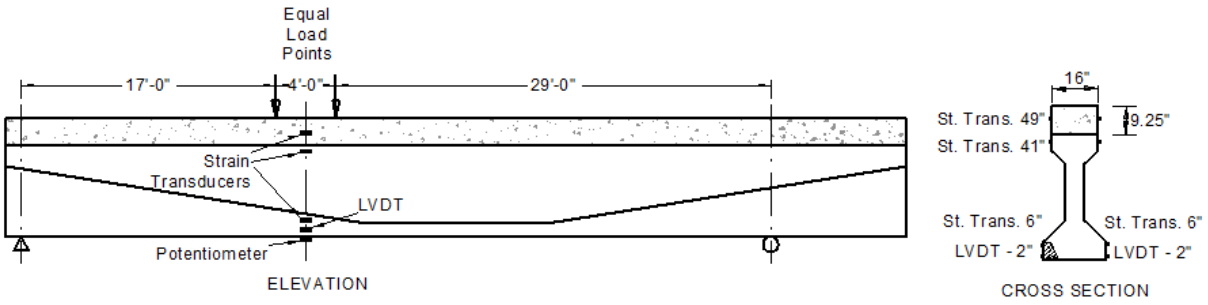

Figure 3.24: Test 4.2 Setup and Instrumentation

The girder was tested on November 20, 2014. Initially, the rate of loading was managed to ensure there were no effects from sudden or impact loading. The load was applied in

approximately 25 kip increments. At each increment, the girder was allowed to settle and cracks were inspected, highlighted, and marked. The test was stopped at a load level of 241 kips and 4.12 in of deflection due to a malfunction of the actuator used for application of load, at which point it appeared as though it would slip out of plumb with the girder. A second iteration of the test was conducted on November 25, 2014. During this iteration, the girder was loaded to a level of 265 kips when failure occurred. Inspection of the specimen after the test led to the observation that the deck concrete had crushed, resulting in a flexural compressive failure as shown in Figure 3.25. Figure 3.26 shows the cracking observed below the load point near the failure load.

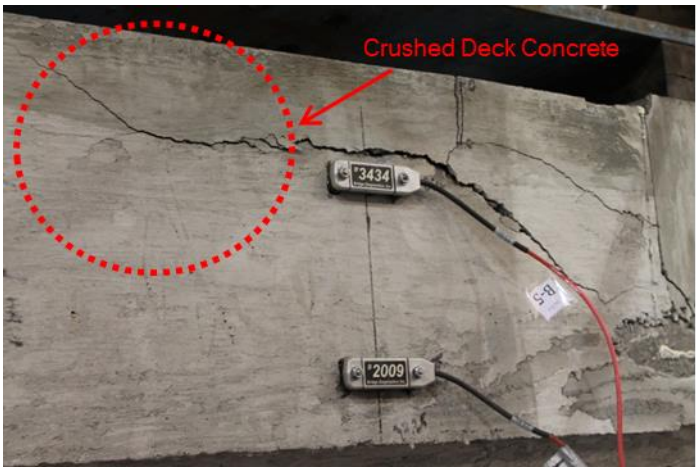

Figure 3.25: Flexural Compression Failure in Test 4

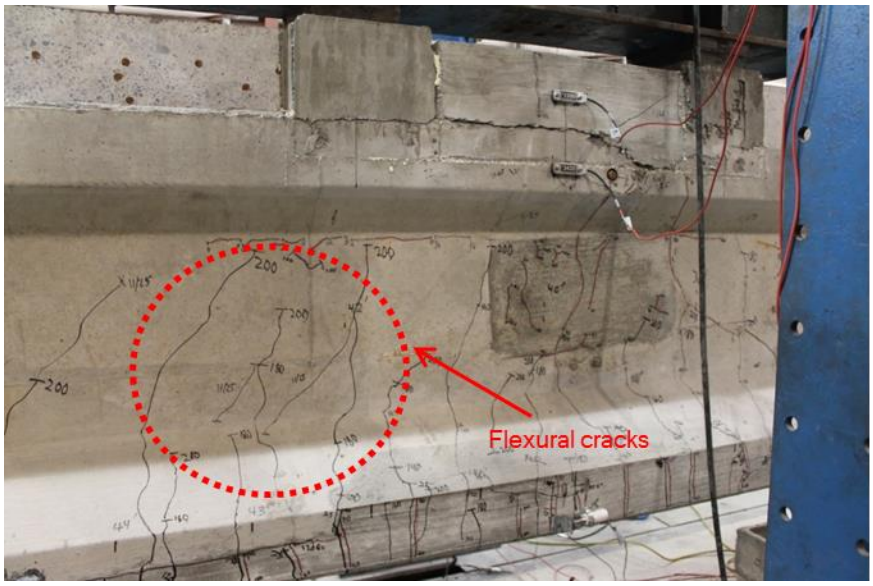

Figure 3.26: Cracking Patterns near Maximum Applied Load in Test 4

3.6 Test 5 – FRCM Repaired Girder with Four Severed Strands

The girder used in both Tests 5 and 6 was damaged a distance of 2 ft on either side at approximately the one-third and two-thirds points along the length of the girder. This corresponds to 4 ft of damage centered at the 20 ft location, and 4 ft of damage centered at the 40 ft location. Of the 48 prestressing strands in the bottom flange of the girder, four were intentionally severed at each location during damaging. Figure 3.27 shows the locations of the strands that were severed during the damaging process. The length of this girder's damage was chosen to be 4 ft in two locations as shown in Figure 3.28. The two damage locations allowed two repair techniques to be tested on the same girder without one repair influencing the other repair's test results.

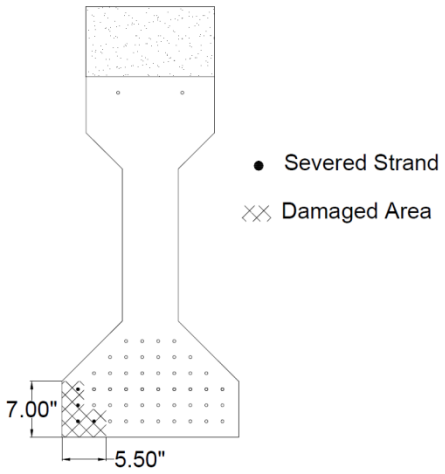

Figure 3.27: Tests 5 and 6 Cross-Section through Damaged Area with Severed Strand Locations Shown

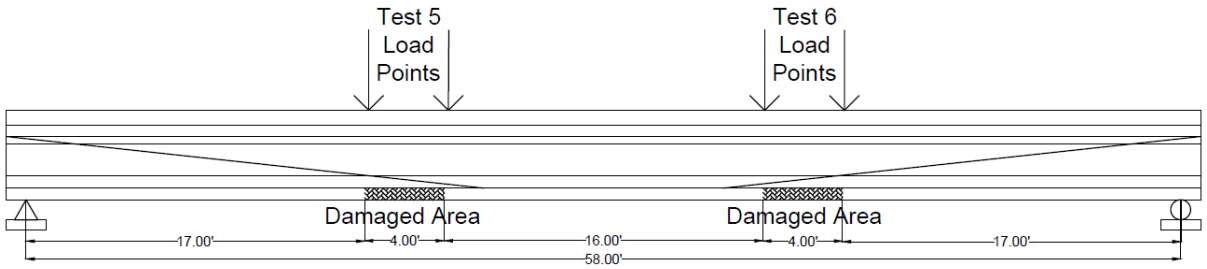

Figure 3.28: Tests 5 and 6 Damage Locations

Professional subcontractors conducted the repair for Test 5 with a high strength, quick set concrete patch and Ruredil X Mesh Gold FRCM composite. Ruredil X Mesh Gold FRCM is a 0.0017 in thick PBO fabric with Ruredil X Mesh M750 mortar (Ruredil X Mesh Gold, 2012). After the concrete patch was placed and allowed to cure, the FRCM was installed. Test 5 was a flexural test of a 52 ft simple span length. Figure 3.29 shows the test setup along the length of the girder. Data was continuously recorded using a high speed data acquisition system. Figure 3.30 shows the instrumentation layout along the length of the girder. Three potentiometers were attached to the bottom of the girder to measure vertical deflection during the test. A 400 kip load cell was placed between the actuator and the load frame to measure the applied load.

Figure 3.29: Test 5 Setup

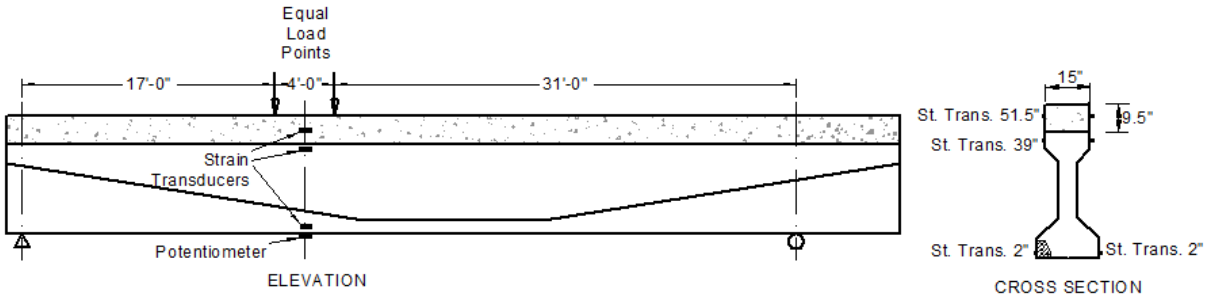

Figure 3.30: Test 5 Setup and Instrumentation

The girder was tested on April 10, 2015. Initially, the rate of loading was managed to ensure there were no effects from sudden or impact loading. The load was applied in approximately 25 kip increments. At each increment, the girder was allowed to settle and cracks were inspected, highlighted, and marked. The test was stopped at a load level of 175 kips and 1.4 in of deflection, due to a malfunction with the actuator used for the application of load appearing to be slightly out of plumb with the rest of the girder. The actuator was unloaded, straightened, and fully reloaded to 175 kips.

During the second run, the test was stopped at a load level of 222 kips and 3.00 in of deflection when it was observed that horizontal shear cracking began to propagate in the deck. Horizontal shear cracking was observed in vicinity of the concrete deck near 1 in saw cuts in the concrete deck that were made when the girder was removed from the rest of the bridge deck. The horizontal shear cracking is shown in Figure 3.31. In order to ensure that test would not fail in horizontal shear and to make sure the region of Test 6 was unaffected, the test was stopped and the saw cuts were filled in with repair concrete. No second attempt of the Test 5 repair was run. The subsequent analysis revealed the strain in the FRCM would not reach a point of failure, and therefore the failure mode would be concrete crushing. It was determined that re-conducting the test would not show more about the FRCM material. Figure 3.32 shows the cracking observed at the load point near the peak load prior to stopping the test.

Figure 3.31: Horizontal Shear Cracking in Deck of Test 5

Figure 3.32: Cracking Patterns near Maximum Applied Load in Test 5

3.7 Test 6 – FRCM Repaired Girder with Four Severed/Re-Tensioned Strands

After testing the three repair methods individually, Test 6 was used to show how repair methods can be used together. The repair method combined an active repair to retension the strands (strand splicing), with a passive tensile repair (externally bonded FRCM). For Test 6, the same girder was used again, with the other four damaged strands being tested. The location of the four severed prestressing strands is shown in Figure 3.27. As shown in Figure 3.28, the girder was damaged at 4ft to allow it to be damaged in two locations.

Professional subcontractors conducted the repair of the damaged location for Test 6 with a high strength, quick set concrete patch, Ruredil X Mesh Gold FRCM composite, and four strand splices. Ruredil X Mesh Gold FRCM is a 0.0017 in thick PBO fabric with Ruredil X Mesh M750 mortar (Ruredil X Mesh Gold, 2012). After the strands were spliced, the concrete patch was placed and allowed to cure. After the concrete patch cured, the FRCM was installed.

Test 6 was a flexural test of a 52 ft simple span length. Figure 3.33 shows the test setup along the length of the girder. Data was continuously recorded using a high speed data acquisition system. Figure 3.34 shows the instrumentation layout along the length of the girder. Three potentiometers were attached to the bottom of the girder to measure vertical deflection during the test. A 400 kip load cell was placed between the actuator and the load frame to measure the applied load.

Figure 3.33: Test 6 Setup

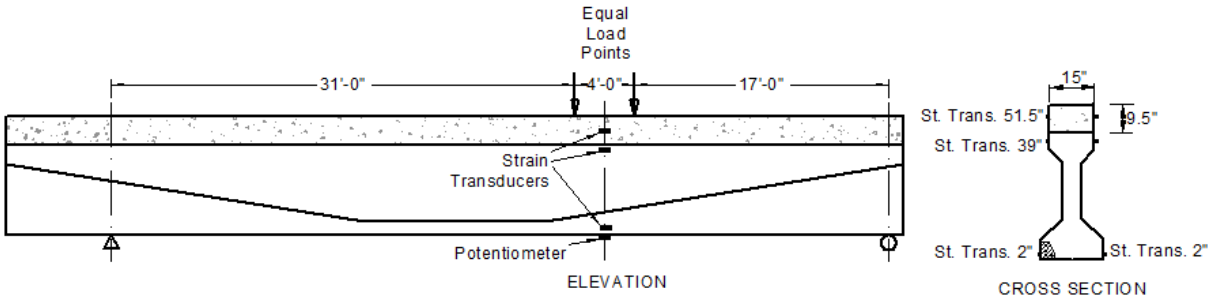

Figure 3.34: Test 6 Setup and Instrumentation

The girder was tested on April 20, 2015. Initially, the rate of loading was managed to ensure there were no effects from sudden or impact loading. The load was applied at approximately 25 kip increment. At each increment, the girder was allowed to settle and cracks were inspected, highlighted, and marked. The test was stopped at a load level of 269 kips and 3.39 in of deflection, when full flexural failure was reached. Inspection of the specimen after the test led to the observation that the compressive deck concrete crushed, resulting in a flexural compressive failure as shown in Figure 3.35. Figure 3.36 shows the cracking observed below the load point near the failure load.

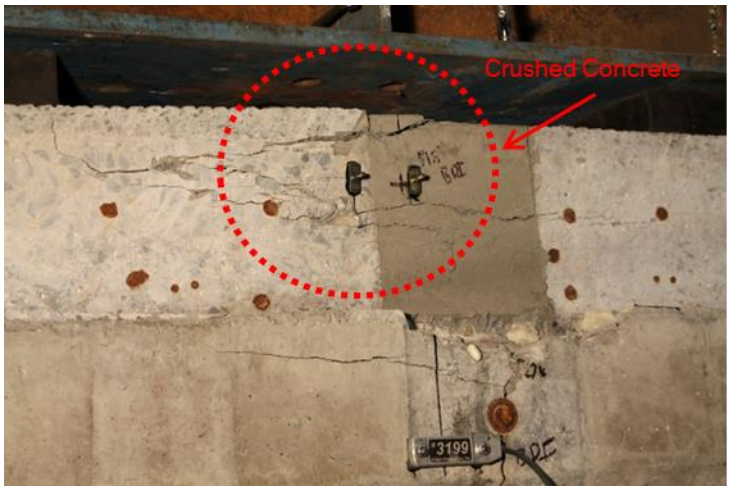

Figure 3.35: Concrete Crushing Failure in Test 6

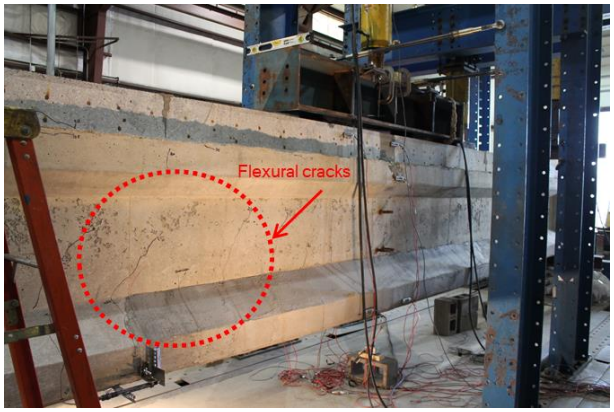

Figure 3.36: Crack Patterns near Maximum Applied Load in Test 6

CHAPTER 4 DESCRIPTION OF ANALYTICAL MODELS

4.1 Introduction

Experimental tests like those presented in Chapter 3 provide unique insights on the impact of collision-induced damage and on the effectiveness of retrofit techniques. Still, experimental tests must always be supplemented with analytical simulations. The analytical models allow for the evaluation of a large number of different configurations, which cannot all be tested experimentally. In the context of the research project described herein, the experimentally tested girders failed almost exclusively due to crushing on the compressive zone of the section. Such failure was induced due to the absence of the deck, which would increase the capacity of the compressive zone in real-life girders. The presence of the deck would probably lead to failure in the tension zone of the section. Thus, numerical models are necessary herein to investigate the performance of damaged and repaired girders which include the effect of the deck.

This chapter describes the analytical models developed for the analysis of damaged and repaired girders. Two types of models have been employed, namely, nonlinear beam models and three-dimensional, continuum-based, finite element models. The nonlinear beam models are attractive for their conceptual simplicity, computational efficiency and their capability to capture the response of flexure-dominated beams. The three-dimensional, continuum-based finite element models can capture – in more detail – certain aspects of the response, such as the confinement effect on concrete and the shear-flexure interaction in bridge girders.

4.2 Description of Nonlinear Beam Models

In the present study, the beam models are defined using the analysis program OpenSees (Mazzoni et al. 2006). The modeling approach employed is schematically summarized in Figure 4.1. Specifically, the length of each girder is modeled using several beam elements, each beam element corresponding to a portion of the girder length. Appropriate restraints are applied to the nodes corresponding to the endpoints of the girder, as also shown in Figure 4.1a. The harped strands in each girder are modeled with nonlinear truss elements. To ensure the compatibility between the strands and the beams at each location along the length of the girder, each nodal point of the truss elements is connected with rigid links to the corresponding nodal point of the beam element.

4.2.1 Sectional Model

The sectional response of the beam elements is obtained using a fiber formulation. Specifically, the cross-section is discretized in multiple fibers, as schematically shown in Figure 4.1b. Each fiber has an assigned area and an assigned uniaxial stress-strain law. At each stage in an analysis, the beam model can provide the reference axial strain, ε_o, and the curvature, φ, at each section. Assuming that a beam is aligned with the x-axis and the sectional depth of the beam is aligned with the y-axis as shown in Figure 4.1, the strain ε_i of each fiber "i" can be calculated using the following expression:

$$\varepsilon_i = \varepsilon_o - \varphi \cdot y \qquad (4.1)$$

The "-" sign in Equation (4.1) is required when positive curvature leads to tension in the bottom fibers of a horizontal beam section.

Given the strain ε_i the uniaxial material law assigned to the fiber "i" gives the stress σ_i of the fiber. Then, given the cross-sectional area A_i of each fiber, the axial force and bending moment of the section is obtained by summing the axial force and bending moment contributions of all the fibers.

$$N = \sum_i (A_i * \sigma_i) \qquad (4.2)$$

$$M = -\sum_i (A_i * \sigma_i * y_i) \qquad (4.3)$$

The approach summarized in Equations (4.1) through (4.3) can be extended in three-dimensional beam analysis. The advantage of a fiber sectional model like the one employed herein is that the axial-flexure interaction of a nonlinear girder can be naturally captured, provided that appropriate uniaxial stress-strain laws are used for the concrete, prestressing strands and retrofit components. The influence of the piece of deck on each girder is accounted for in the beam models. The thickness of the piece of deck is equal to 8.75 in and the width of the deck is equal to the flange width of the girder section.

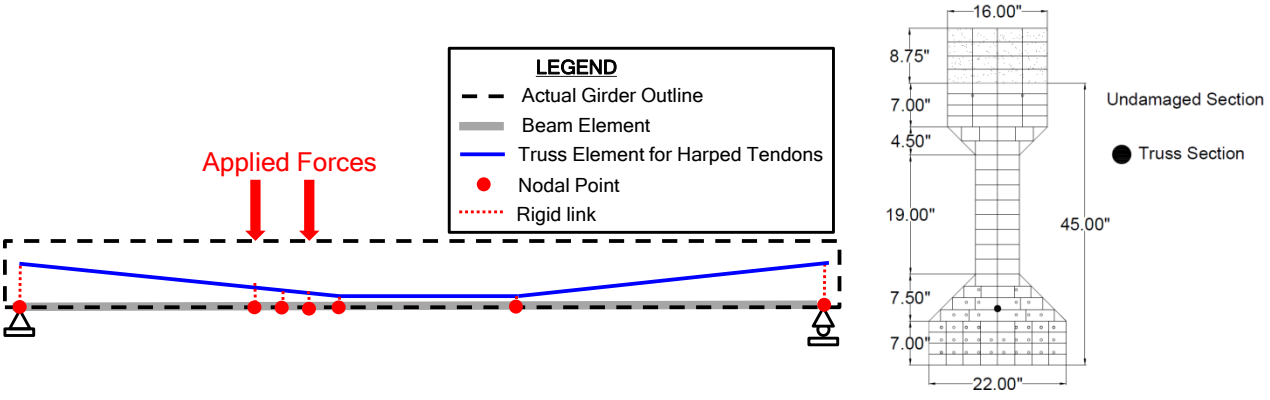

a) Model Layout **b) Fiber Sectional Model**

Figure 4.1: Schematic Description of Nonlinear Beam Model

4.2.2 Material Models and Calibration of Material Properties in Beam Models

4.2.2.1 Concrete and Strands

The concrete in the girder is modeled using the Hognestad material law (e.g., Hisham and Mohd 1994), summarized in Figure 4.2a, which can account for the effect of tensile strength degradation due to cracking, compressive strength degradation due to crushing, and for the stiffness degradation due to damage in the material.

The material in the steel prestressing strands is described with an elastoplastic law having linear kinematic hardening. For monotonic uniaxial loading, such elastoplastic law leads to a bilinear shape of the stress-strain curve, as shown in Figure 4.2b. An initial autogenous strain is defined for the material of each strand, such that the strand stress was equal to the estimated value of actual prestress in the bridge girders. The prestress in the strands is assumed to be 140 ksi, a value verified by material testing.

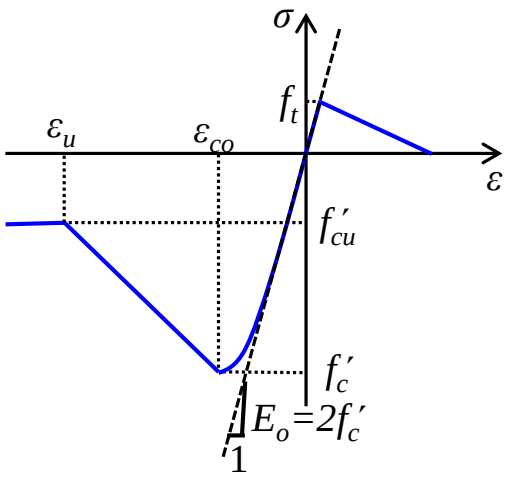

a) Hognestad Concrete Material Model (Hisham & Mohd, 1994)

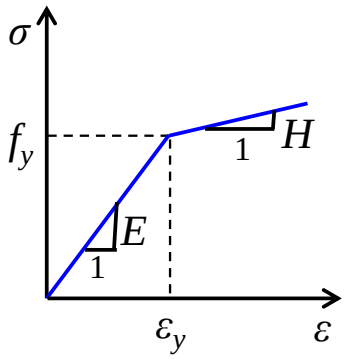

b) Elastoplastic Material Model With Linear Kinematic Hardening for Strands

Figure 4.2: Uniaxial Material Laws used in Beam Models

Several initial analyses were conducted using nominal material properties, i.e., a compressive strength of 5 ksi for the concrete and a yield stress of 225 ksi for the strands. The

subsequent availability of material test data on the girder and deck concrete and on the strands allowed the modification of the calibration to match the experimentally obtained material strength values. The calibrated uniaxial stress-strain laws for the concrete in the girder and in the deck are presented in Figure 4.3a, while the calibrated model stress-strain curve of the strand material is compared to the experimentally obtained curve in Figure 4.3b.

The steel strands have an initial elastic modulus E = 27,000 ksi, with a yield stress of F_y = 243 ksi at a strain of 0.009, and a tangent modulus of H = 540 ksi. The failure strain is set to 0.05 at an ultimate strength of f_{pu} = 264 ksi. Initial prestress is f_{pe} = 140 ksi, corresponding to a strain of 0.00519. For the beam concrete, the peak compressive strength is f_c' = 6.65 ksi, while for the deck concrete the compressive strength is f_c' = 6.02 ksi. For both concrete models, the peak tensile strength, f_t, was taken as 10% of the compressive strength, the residual compressive strength, f_{cu}', is 85% of the compressive strength at a strain of ε_u = -0.003, and the peak compressive strength occurs at ε_{co} = -0.002.

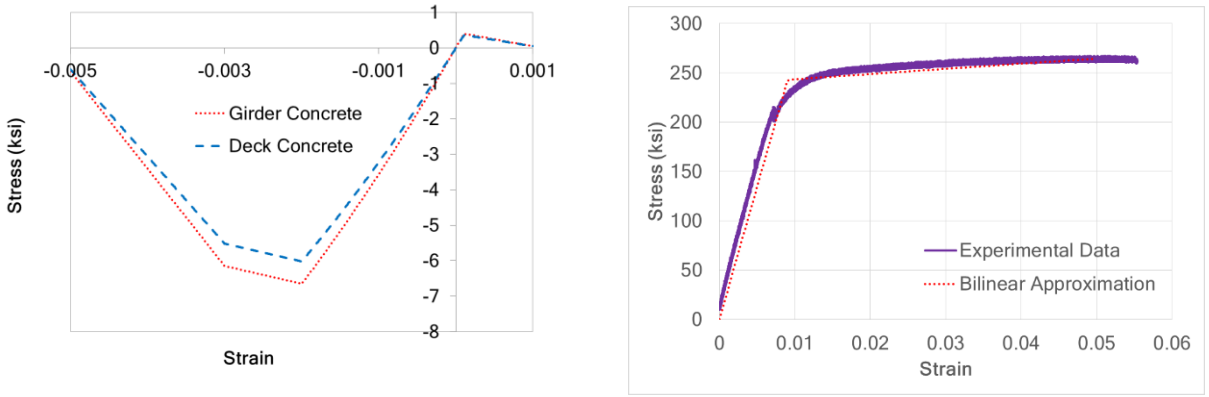

a) Hognestad Concrete Material Model (Hisham & Mohd, 1994)

b) Calibration of Steel Strand Material Model With Material Test Data

Figure 4.3: Calibrated Material Laws for Concrete and Steel

4.2.2.2 Strand Splices

The splices are modeled using a multilinear elastoplastic material law. The specific law allows the user to define a stress-strain curve consisting of multiple linear segments, and to explicitly capture the effect of material strength degradation due to, e.g., fracture. The prestressing force restored and the ultimate strength of the strands are governed by uncertainty. In the present study, and given that the splices had been installed with a 150 ft-lbs torque, the prestressing in the spliced strands is assumed to equal 200 ksi, i.e., 0.8 f_{pu}, in accordance with the manufacturer's recommendation (Prestress Supply Incorporated, 2010).

Given the inherent uncertainty in the ultimate strength of the splices, several alternative hypotheses have been examined. The lower bound of splice strength is assumed to be 212.5 ksi (0.85 f_{pu}) and the upper bound is assumed to be 250ksi (f_{pu}).

Figure 4.4a presents the stress-strain curves of the spliced strands for different values of splice failure stress. These curves have been obtained on the basis of the assumption that the spliced strands have the same stress-strain behavior as the undamaged strands and that splice failure leads to sudden strength degradation. It is worth noting that the curve corresponding to failure at 250 ksi differs from that of the undamaged strands. Specifically, the nominal strength of the strands is 250 ksi, and the bilinear stress-strain curve reaches this value at a strain of 0.022. The curve of the undamaged strands, shown in Figure 4.3b, reaches higher stresses than 250 ksi, i.e., it reaches a stress of 264 ksi at a strain of 0.05.

4.2.2.3 FRP Overlays

The FRP material overlays are also modeled using a multilinear stress-strain curve. The stress-strain curve of the overlays is established using data from the manufacturer. The modulus of elasticity is E_f = 10,700 ksi and the rupture strain for an overlay is ε_{fu} = 0.014. The possibility for debonding of the overlays also needs to be accounted for by the models.

FRP end peeling (also referred to as plate-end debonding) can result from the normal stresses developed at the ends of externally bonded FRP reinforcement. With this type of debonding, the existing internal reinforcing steel essentially acts as a bond breaker in a horizontal plane, and the concrete cover pulls away from the rest of the beam (Teng et al. 2002). The possibility of such a failure is evaluated in Appendix B using the ACI 440 2R.08 document (ACI 2008). The calculations in the appendix lead to the conclusion that plate-end debonding is not probable. Therefore, it is not examined further in the analytical models of the present study.

Another possible failure mode is intermediate crack-induced debonding. This happens when debonding (loss of adhesive strength) occurs in the vicinity of a crack away from the end regions of the overlays, and he debonding crack propagates then towards the end region of the overlay. The ACI 440 2R.08 document (ACI 2008) provides guidelines to estimate the effective strain, ε_{fd}, at which such debonding can occur. The calculations are presented in Appendix B and give a value ε_{fd} = 0.0052. Since this strain value is less than the rupture strain of the FRP, intermediate crack-induced debonding is deemed as the most probable failure mode. The stress-strain curve used for the FRP material is presented in Figure 4.4b. The figure compares the stress-strain curve corresponding to full strength, i.e., to rupture of the FRP, and the curve corresponding to intermediate crack-induced debonding, which is used in the numerical models.

4.2.2.4 FRCM Overlays

The behavior of the FRCM overlays is also described using a multi-linear material law. Two alternative stress-strain curves are employed in the present study. The first curve is based on information provided by the manufacturer of the material. According to the manufacturer, the thickness of each FRCM strip is t_f = 0.0018 in, the modulus of elasticity is E_f = 39,200 ksi, and the strain at rupture is ε_{fu} = 0.021. The second curve has been obtained from experimental tests conducted at the University of Miami (Pino and Nanni 2015). The ACI 549.4R-13 document (ACI 2013) establishes an idealized stress-strain curve for FRCM overlays, as shown in Figure 4.5a. The idealized curve consists of two linear segments. The first linear segment corresponds to the initial stage of behavior. After the strain exceeds a transition strain value, shown in Figure 4.5a, the slope of the idealized stress-strain law reduced. Using the material test data, Pino and Nanni (2015) established a stress-strain curve similar to that proposed in ACI 549.4R-13. The transition point corresponds to strain and stress values of 0.00017 and 54 ksi, respectfully, while the failure corresponds to a strain of 0.017 and a stress of 241 ksi.

The possible failure modes for FRCM overlays are shear/tension delamination of the concrete cover, debonding of the FRCM from the concrete substrate, interlaminar debonding, or slippage of the mesh with the cementitious matrix. The ACI 549.4R-13 document (ACI 2013) states that to account for these failure modes, the effective tensile strain level in the FRCM reinforcement attained at failure, ε_{fe}, should be limited to the design tensile strain of the FRCM composite material, ε_{fd}, defined as $\varepsilon_{fe} = \varepsilon_{fd} \leq 0.012$. Therefore, in the model, the failure strain of the FRCM material was set to be 0.012.

The two alternative curves employed for the FRCM, i.e., the one provided by the manufacturer and the one obtained from experimental tests, have been modified to have failure at strain of 0.012, and are shown in Figure 4.5b.

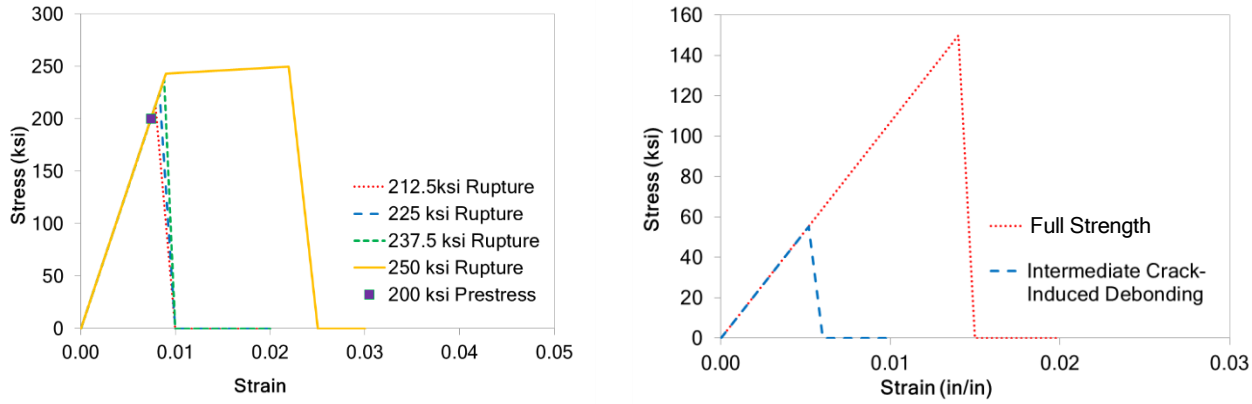

a) Spliced strand stress-strain curves corresponding to different levels of splice failure

b) FRP overlay stress-strain curves corresponding to full fiber strength and to debonding

Figure 4.4: Uniaxial Material Laws for Retrofit Materials

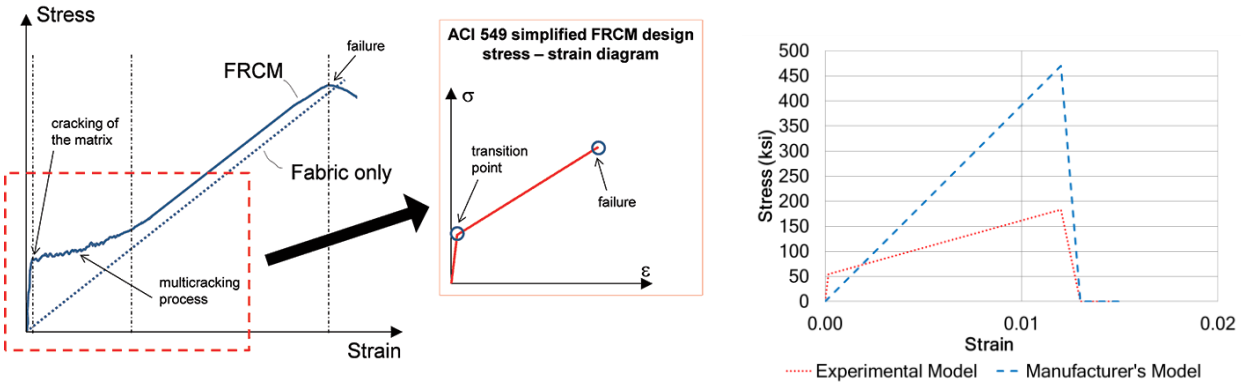

a) Idealized stress-strain curve (Tumialan 2014)

b) Alternative stress-strain curves employed in the present study

Figure 4.5: Uniaxial Material Laws for FRCM

4.2.2.5 Solution Procedure

In the analysis procedure, the self-weight of each girder is initially applied as a distributed loading. The additional concentrated loads, e.g., the applied forces in the experimental tests, are then applied on the models. An incremental procedure is used in the analysis, i.e. the solution is conducted for multiple steps, with the applied loadings being incrementally changed at each step. A Newton-Raphson iterative scheme is employed to satisfy the nonlinear equations of equilibrium. Given that strength degradation is expected to occur in the analytical models pursued herein, a displacement-control algorithm (McGuire & Gallagher, 2015) is used. In this algorithm, a constrained equation is enforced in each solution step, i.e., that the load increments are such that a selected nodal displacement acquires a target value in each step. The use of a displacement-control algorithm allows the solution to proceed and converge at each step, even when strength degradation occurs in the analysis.

4.3 Description of Continuum-Based Finite Element Models

The three-dimensional, continuum-based, finite element (FE) analyses of the damaged and repaired bridge girders are conducted using the commercial program LS-DYNA (Hallquist, 2007). A schematic presentation of a three-dimensional continuum FE model is presented in Figure 4.6. As seen in the figure, the model explicitly accounts for the loading apparatus (i.e., the presence of a spreader beam) by means of additional elastic solid elements. The prestressing strands are modeled using truss elements with an appropriate uniaxial stress-strain law.

The damaged and repaired regions of the girders are explicitly modeled in the simulations, using appropriate material models and elements. The retrofit overlays, i.e., the FRP strips and the FRCM layers, are modeled through the superposition of shell elements on the appropriate locations of the model. Given that the presence of the saw cuts at the compressive zone of the girders affected the response of several test specimens, these cuts are accounted for in the finite element analyses.

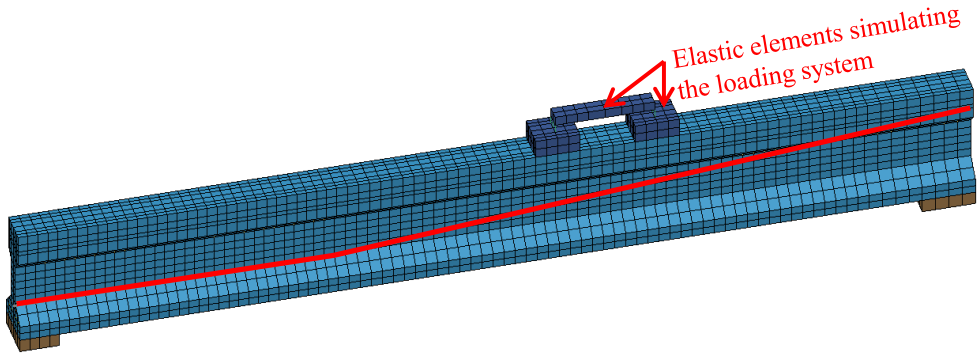

Figure 4.6: Schematic Presentation of Continuum-based Finite Element Model of Bridge Girder, in which the truss elements representing the harped strands are highlighted

4.3.1 Continuum-Based Finite Element Model Material Properties

The behavior of the concrete in the girders and in the repair patches is described using the Winfrith material model (Broadhouse, 1995). The specific material model is based on the yield surface proposed by Ottosen, capturing the effect of biaxial and triaxial stress states on the compressive strength of the material (Ottosen, 1977). The effect of tensile strength degradation due to cracking is also accounted for by the model.

The material model allows the definition of a compressive failure strain, i.e. the strain at which the concrete is assumed to be fully crushed. In the present study, this failure strain is set equal to -0.003. For this model the girder concrete is assumed for the entire cross-section for simplicity, though this is not a conservative assumption. Figure 4.7 shows the concrete material model used for the solid elements in the continuum-based finite element analysis.

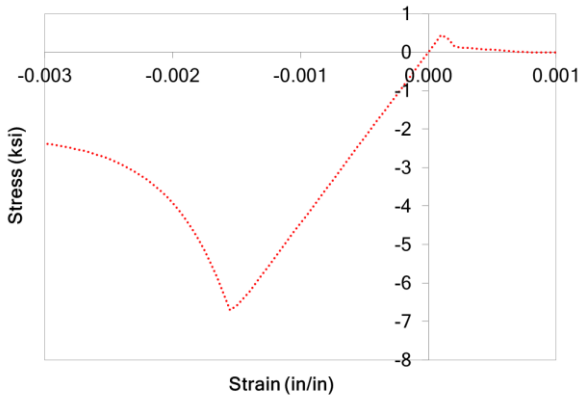

Figure 4.7: Concrete Material Uniaxial Stress-Strain for Continuum-Based FE Models

The material of the strands for the FE models is described by an elastoplastic law with linear kinematic hardening, calibrated in an identical fashion as that for the beam models. The target prestress in the strands is obtained in the tests by defining a temperature increase in the

models, which in turn created the autogenous strain required to generate the prestress of each strand.

An elastoplastic material with linear kinematic hardening is also used to model the strand splices. The analysis software allows the definition of a failure strain, i.e. the value of plastic strain at which the material loses its resistance. By appropriately defining the value of the failure strain, the present study could account for the failure of the strand splices for various levels of tensile strain.

The FRP is modeled in LS-DYNA using an enhanced version of the brittle damage model by Chang and Chang for composite materials (Chang & Chang, 1987). The specific material model can account for the orthotropic nature of an FRP strip, i.e. for the different strength and stiffness properties for the directions parallel and perpendicular to the fibers. Additionally, the model can account for different material strength values depending on the loading directions. The shell elements simulating the FRP overlays include – as different layers – both the strips whose fibers are aligned with the axis of the girder specimen and the transverse strips. For each FRP layer, the strength in the fiber direction is determined in accordance with the procedure employed for the beam models. The strength in the direction perpendicular to the fibers is assumed to be 10% of the peak strength of the strip.

The constitutive model by Chang and Chang is also used to describe the behavior of the FRCM overlays (Chang & Chang, 1987). The transverse fiber area of the FRCM is about 25% of the corresponding area of the longitudinal fibers, i.e. the fibers which were aligned with the axis of the specimens. For this reason, the strength for the transverse direction of the FRCM overlays is set to 25% of the corresponding strength in the longitudinal direction.

CHAPTER 5 VALIDATION OF ANALYSIS METHODS

5.1 Introduction

This section compares the tested and calculated data from the reported tests. In the analyses presented herein, the self-weight of the beam was initially applied as a distributed loading. Subsequently, the concentrated applied forces were introduced in the model. Since the deflection due to the self-weight of the specimens was present in the unloaded state of the beams, the reported analytical results provide values of the additional deflection due to the concentrated loadings. In other words, the effect of the deflection due to self-weight of the girders is removed from the analytical results. The load-deflection response from each test is presented and the ability of both the nonlinear beam models and continuum-based finite element models to predict those responses is discussed.

5.2 Validation of Nonlinear Beam Models

The results of the validation analyses using the beam models for the first test are presented in Figure 5.1a for Test 1.1 and Figure 5.1b for Test 1.2. The failure mode for both analyses is concrete crushing in the deck. This is indicated by the fact that at peak load, the strain in the concrete fiber at the top of the deck reaches -0.003, the ACI indicator of crushed concrete (ACI , 2008). Both analyses agree well with the experimental data, especially the second iteration which is more important to modeling because there was no equipment failure to affect the experimental results. The good agreement is based on the ability of the model to predict the initial elastic slope, the load at first cracking, the post cracking slope, and the peak load at failure.

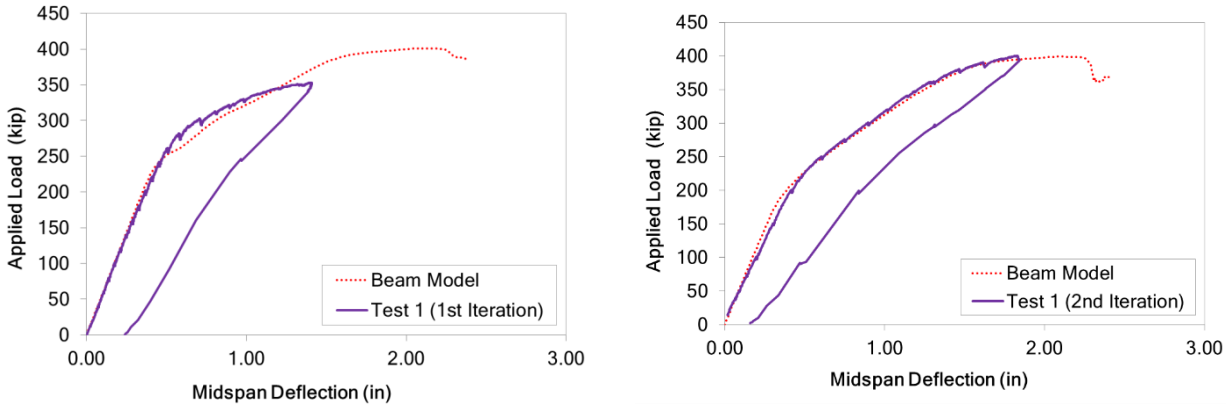

a) Test 1.1 **b) Test 1.2**

Figure 5.1: Comparison of Experimentally and Analytically Obtained Load-Deflection Curves for Test 1.

The analyses for Test 2 are conducted for four different values of strand splice strength. The first analysis run is at the lower bound of splice strength, 212.5 ksi (0.85 f_{pu}). The second analysis is at 225 ksi (0.9 f_{pu}) splice strength. The third analysis is at 237.5 ksi (0.95 f_{pu}) splice strength, while the fourth analysis is at the upper bound of splice strength at 250 ksi (f_{pu}). The results of these analyses are shown in Figure 5.2a. The failure mode for the first three analyses is strand splice rupture. This is indicated by the fact that at peak load, the stress in the repaired steel strand fiber reaches the specified splice strength, and then begins to decrease as load drops. The fourth analysis, though, with splice strength at full 250 ksi, fails in concrete crushing mode, with the strain in the concrete fiber at the top of the deck reaching -0.003.

Both the second and third analyses agree well with the experimental data, especially the peak load from the 225 ksi analysis, and the predicted maximum deflection from the 237.5 ksi analysis. Based on the analysis results, the 212.5 ksi failure strength for strand splices underpredicts the strength of the repair, while the 250 ksi failure strength overpredicts the strength. The 225 ksi and 237.5 ksi models are so close that one cannot be chosen by using nonlinear beam models alone. The more refined, continuum-based, finite element analyses

discussed in the following section allows for the selection of a unique curve for the spliced strands.

Two analyses are conducted for Test 3, using alternative stress-strain curves for the FRP overlay. The first analysis run is at the intermediate crack-induced debonding failure scenario. The failure mode for this analysis is FRP debonding, indicated by the fact that at the peak load, the strain in the FRP layer reaches $\varepsilon_{fd} = 0.005173$. The second analysis is at the full flexure failure scenario. The failure mode for this analysis is concrete crushing, at which point the strain in the concrete fiber at the top of the deck reaches -0.003, the ACI indicator of crushed concrete. The results of these analyses are shown in Figure 5.2b.

Both analyses agree well with the experimental data. Since the peak load of the debonding mode corresponds to a deflection of 3.15 inches, which is the deflection at the end of the test, it cannot be determined which material model is to be used for the FRP repair. Such decision is rendered possible by the more refined finite element analyses presented in the following section.

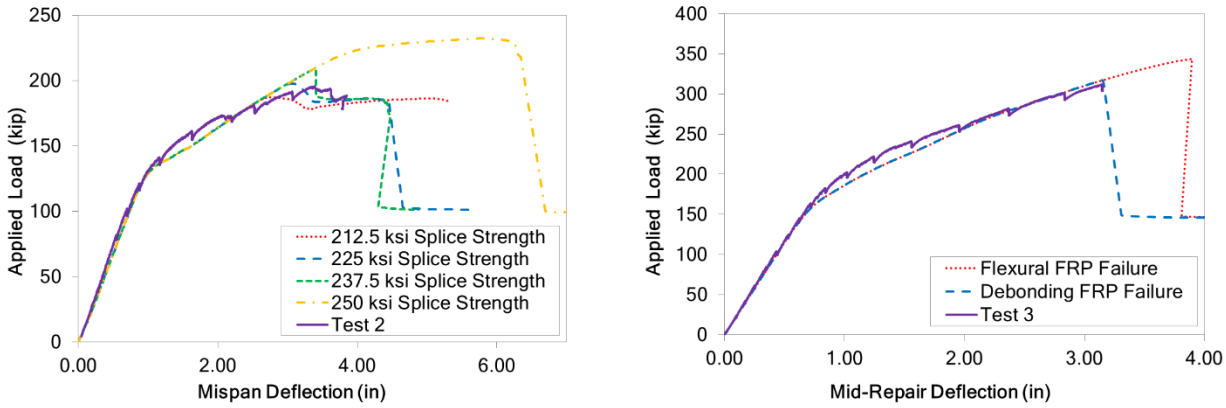

a) Test 2 **b) Test 3**

Figure 5.2 : Comparison of Experimentally and Analytically Obtained Load-Deflection Curves for Tests 2 and 3.

For the nonlinear beam model of Test 4, the four analyses run are with the two different splice strengths, with the two different iterations of the test setup. Since the failure of Test 4.2 was concrete crushing and splice rupture was not seen, it is assumed that the splice strength had been fully restored to 250 ksi (f_{pu}). The splice model from the Test 2 splice repair is taken to be the more conservative rupture at 225 ksi (0.9 f_{pu}) curve. Modeled in these analyses are the two most likely splice strengths: 225 ksi (0.9 f_{pu}) and 250 ksi (f_{pu}).

The first set of analyses run are the first iteration of the test, Test 4.1, in which the span was 58 ft and the beam was loaded to 241 kips before it became apparent that the girder was becoming out of plum. The results of the analyses of this load setup with splice strength of 225 ksi (0.9 f_{pu}) and 250 ksi (f_{pu}) is shown in Figure 5.3a. The second set of analyses run are the second iteration of the test, Test 4.2, in which the span was changed to 50 ft and the girder was loaded to concrete crushing failure. Cracking due to previous testing is accounted for by loading the model to 241 kips, unloading it, and then recording the load-deflection response. The results from this second analysis are shown in Figure 5.3b.

The failure mode for both iterations at 225 ksi splice strength is strand splice rupture, while at 250 ksi splice strength, it was concrete crushing. This indicated that the 250 ksi splice strength model is more appropriate for this scenario because the failure mode in the Test 4.2 was concrete crushing. It is valid to assume that the 250 ksi failure strength for strand splices is the correct model to use for a four strand splice repair.

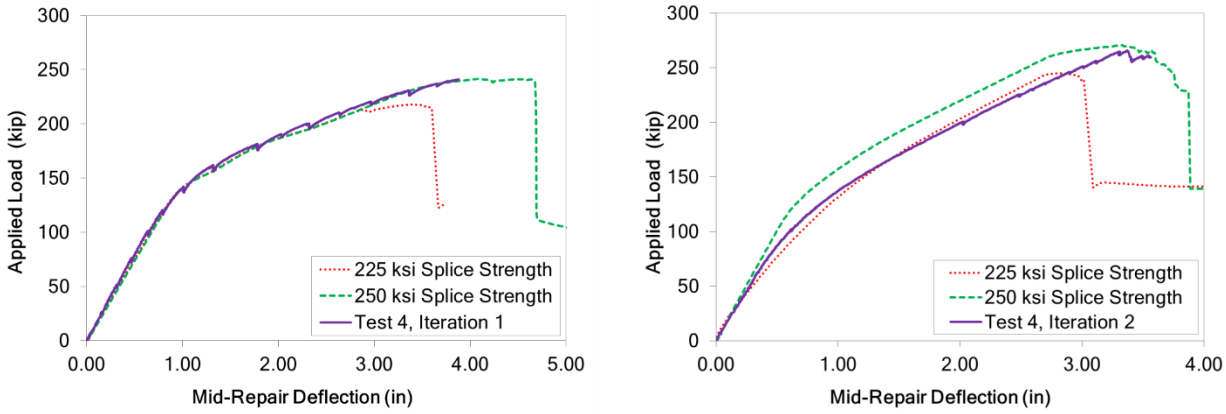

a) Test 4.1 **b) Test 4.2**

Figure 5.3: Comparison of Experimentally and Analytically Obtained Load-Deflection Curves for Test 4.

The analyses for Test 5 are conducted with two different FRCM material model scenarios. The first analysis run is the elastic manufacturer's material law scenario. The second analysis run is the bilinear experimentally derived material law scenario. The failure mode of both analyses is concrete crushing, at which point the strain in the concrete fiber at the top of the deck reaches -0.003, the ACI indicator of crushed concrete. The result of these analyses is presented in Figure 5.4. Both analyses agree well with the experimental data up until the point when the girder was unloaded at 180 kips. From observation, after this unloading and reloading process, horizontal shear cracking occurred, and less deck was effectively present to carry compressive load. Due to the inability of the model to account for the horizontal shear cracking effect, the analyses overpredict the experimental load-deflection response. Since the issues with horizontal shear cracking occurred, it is inconclusive from these analyses which model predicts behavior better.

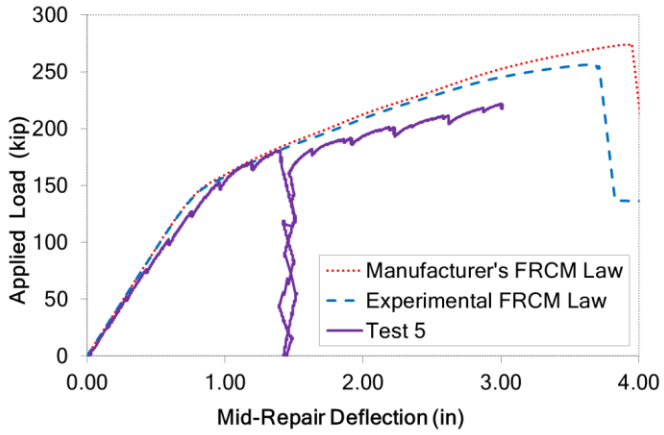

Figure 5.4: Load-Deflection Response of Test 5 vs. Nonlinear Beam Models.

For the nonlinear beam model of the sixth and final test, the four analyses run are with the two different splice material model scenarios and the two different FRCM material model scenarios. The first set of analyses run is run with the manufacturer's FRCM law and the two splice strengths of 225 ksi (0.9 f_{pu}) and 250 ksi (f_{pu}). The second set of analyses is run with the experimentally derived FRCM law and the two splice strengths. In all analyses, the failure mode is concrete crushing, at which point the strain in the concrete fiber at the top of the deck reaches -0.003, the ACI indicator of crushed concrete. The failure modes are surprising for two analyses with splice strength of 225 ksi. Although the splices ruptured during the analysis, as expected, the FRCM had enough residual tensile strength to allow full flexural failure. The results of the manufacturer's FRCM law analyses are shown in Figure 5.5a, while the experimental FRCM law analyses are shown in Figure 5.5b.

The two analyses at 250 ksi splice strength agrees well with the experimental, while the analyses with 225 ksi splice strength underpredict the strength. The difference in the two FRCM material laws is not substantial enough to determine which to material model is to be used for the

FRCM repair. Such decision is rendered possible by the more refined finite element analyses presented in the following section.

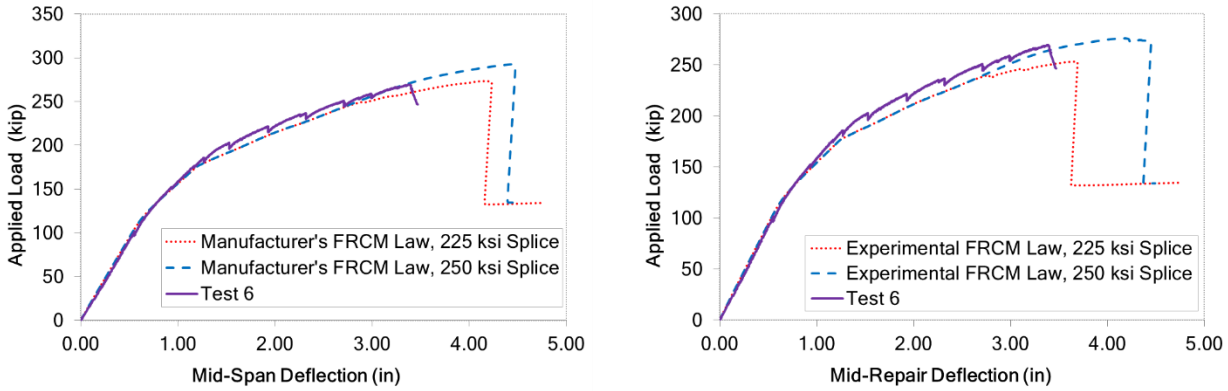

a) FRCM law based on manufacturer's data **b) FRCM law based on material test data**

Figure 5.5: Comparison of Experimentally and Analytically Obtained Load-Deflection Curves for Test 6.

5.3 Validation of Continuum-Based Finite Element Models

A single analysis is conducted for the validation of the three-dimensional continuum-based finite element model of the first test, due to difficulties in establishing the exact loading scenario of the test. The analytical model is validated by the combination of the curves of both iterations of Test 1, which show the initial cracking in the first iteration and the post-cracking behavior in the second iteration. The failure of the continuum-based finite element model is, just as in the nonlinear beam model, concrete crushing. Figure 5.6 shows the continuum-based FE model with concrete solid elements removed that have reached failure strain of -0.003, indicating crushing. The results of this analysis are shown in Figure 5.7a. The continuum-based FE model agrees well with the experimental data, though slightly over-predicts the girder strength.

For the Test 2 continuum-based finite element model, the two analyses run are with the two different splice strength scenarios. The first analysis run is at 225 ksi (0.9 f_{pu}) splice

strength, while the second analysis is at 237.5 ksi (0.95 f_{pu}) splice strength. The results of this analysis are shown in Figure 5.7b. The failure of both continuum-based FE models is not strand rupture as in the nonlinear beam models, but concrete crushing. It can be seen in the load-deflection plot that the girder loses strength with the splice rupture, but has enough residual tensile strength with those elements removed to continue until full flexural failure. Both of the continuum-based FE analyses agree with the experimental data up until the peak load and predicted the splice elements rupturing. For the purposes of being conservative, in the case of eight strands spliced, the model for the strand splices to be used for subsequent analyses is splice rupture at 225 ksi (0.9 f_{pu}) strength.

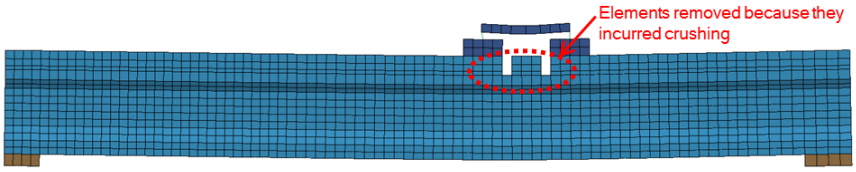

Figure 5.6: Deformed Test 1 Continuum FE Model at End of Analysis

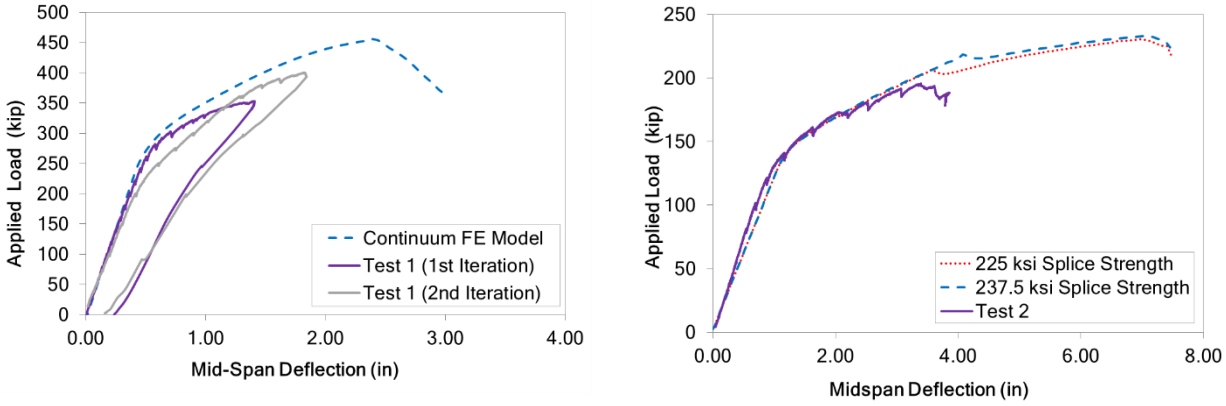

a) Test 1 **b) Test 2**

Figure 5.7: Comparison of Experimentally and Analytically Obtained Load-Deflection Curves for Tests 1 and 2.

The two analyses for the continuum-based FE model of Test 3 are run using alternative stress-strain curves for the FRP overlay. The first analysis run is the intermediate crack-induced debonding failure scenario, and the second analysis is the full flexure failure scenario. The results of this analysis are shown in Figure 5.8a. Both analyses surprisingly show concrete crushing failure mode. This is due to the fact that, even with the debonding stress-strain model, there is shown to be redistribution of stresses in the shell elements when debonding is reached in one shell. Due to the redistribution of stresses, further strength is able to be achieved until flexural failure. Both the analyses agree with the experimental data. Since both analyses show the same strength, it is conservative to assume the use of the intermediate crack-induced debonding strength model to be the appropriate model for subsequent analyses.

For the Test 4 continuum-based finite element model, the only analysis run is the Test 4, Iteration 1 support condition with strand splice strength of 250 ksi (f_{pu}). The results of this analysis are shown in Figure 5.8a. The failure of the FE model is, just as in the nonlinear beam model, concrete crushing. It is valid to assume that for the case of four strands spliced, the model for the strand splices to be used for subsequent analyses is the one with splice rupture at 250 ksi (f_{pu}) strength.

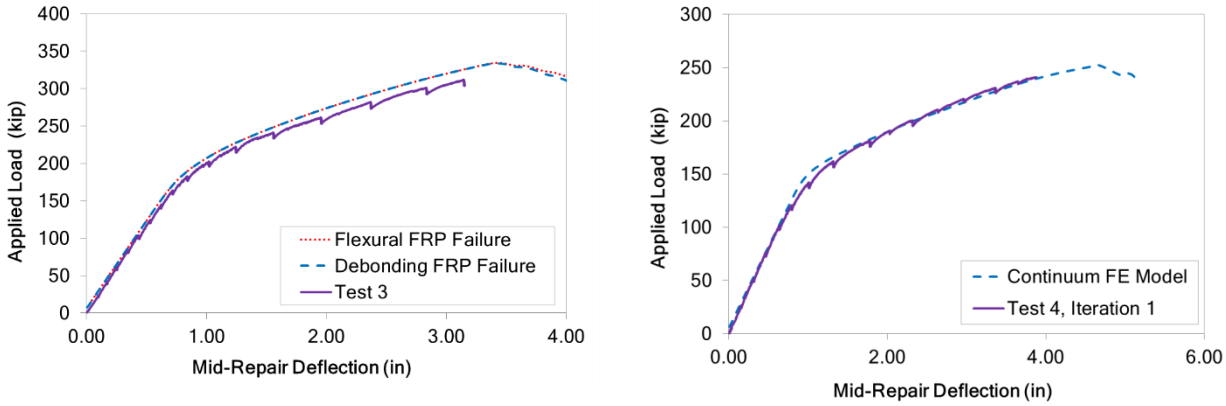

a) Test 3 **b) Test 4.1**

Figure 5.8: Comparison of Experimentally and Analytically Obtained Load-Deflection Curves for Tests 3 and 4.1.

The two analyses for the continuum-based FE model of Test 5 are run using two alternative material laws for the FRCM overlay. The first analysis run is the elastic manufacturer's material law scenario. The second analysis run is the bilinear experimentally derived material law scenario. The results of this analysis are shown in Figure 5.9a. Both analyses give failure due to concrete crushing. The effect of the modeled saw cuts is evident in the analyses. At the saw cut locations, concrete deck elements fail in a different manner than in the experimental test. Similar to the nonlinear beam analyses, both continuum-based FE analyses agree with the experimental data up until the point when the beam was unloaded at 180 kips. It remains probable that this point was when the horizontal shear cracking occurred. The horizontal shear cracking led to less deck being effectively present to carry compressive load, causing a decreased load-deflection response than expected.

For the continuum-based finite element model of the sixth and final test, the two analyses run are with the two different FRCM material law scenarios. Both analyses use a 250 ksi strand

splice strength, as was previously determined to be the more accurate model for four strands spliced. The first analysis run is the elastic manufacturer's material law scenario. The second analysis run is the bilinear experimentally derived material law scenario. The results of this analysis are shown in Figure 5.9n. Both analyses show concrete crushing failure mode. Just as in the nonlinear beam analyses, both analyses agree with the experimental data.

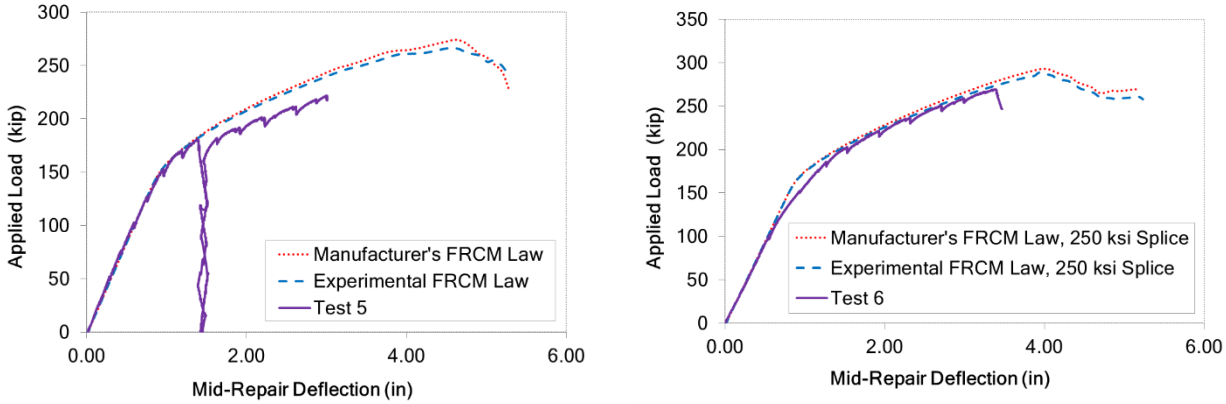

a) Test 5 **b) Test 6**

Figure 5.9: Comparison of Experimentally and Analytically Obtained Load-Deflection Curves for Tests 5 and 6.

5.4 Summary of Results and Discussion

A summary comparison between the experimental tests and the validation analyses using the beam models is presented in Table 5.1. A similar comparison is summarized in Table 5.2 for the FE models. An ideal model is able to predict the initial elastic behavior (initial slope and strength at first cracking), while also being able to predict the failure (failure mode, peak strength, and deflection at failure). Overall, the beam models provided very satisfactory estimates of the peak strength and the deflection at failure for all the girders. The same applies for the finite element models. The synergism of the two models is worth mentioning.

Specifically, the conceptually simpler beam models allowed to reduce the number of alternative stress-strain curves for the strand splices to be used in the more refined and demanding finite element analyses.

Table 5.1: Summary of Comparison Between Experimental Test Results and Beam Models

Analysis	Experimental Peak Load (kips)	Experimental Maximum Deflection (in)	Predicted Load at Maximum Deflection (kips)	Error (%)	Model Predicted Peak Load (kip)	Model Predicted Maximum Deflection (in)
Test 1, Iteration 1	353	1.41	372	5.5	401	2.08
Test 1, Iteration 2	400	1.82	394	-1.4	399	2.08
Test 2, 212.5 ksi	195	3.39	179	-8.4	187	2.75
Test 2, 225 ksi	195	3.39	184	-6	198	3.05
Test 2, 237.5 ksi	195	3.39	208	6.3	208	3.4
Test 2, 250 ksi	195	3.39	209	7.1	232	3.78
Test 3, Debond	311	3.15	317	1.9	317	3.15
Test 3, Flexure	311	3.15	317	2	344	3.9
Test 4.1 (225 ksi)	241	3.88	125	-48.1	218	3.42
Test 4.1 (250 ksi)	241	3.88	240	-0.6	241	4.51
Test 4.2 (225 ksi)	265	3.38	143	-45.9	245	2.85
Test 4.2 (250 ksi)	265	3.38	269	1.4	270	3.32
Test 5, Manufacturer	221	3.00	252	14.3	274	3.94
Test 5, Experimental	221	3.00	245	11.0	256	3.65
Test 6, Man./ 225ksi	269	3.39	260	-3.3	273	4.17
Test 6, Man./ 250ksi	269	3.39	271	0.9	293	4.45
Test 6, Exp./ 225ksi	269	3.39	250	-7.1	253	3.66
Test 6, Exp./ 250ksi	269	3.39	264	-1.8	276	4.18

Table 5.2: Summary of Comparison Between Experimental Test Results and Finite Element Models

Analysis	Experimental Peak Load (kips)	Experimental Maximum Deflection (in)	Predicted Load at Maximum Deflection (kips)	Error (%)	Model Predicted Peak Load (kip)	Model Predicted Maximum Deflection (in)
Test 1	400	1.82	427	6.7	456	2.39
Test 2, 225 ksi	195	3.39	202	3.4	230	6.99
Test 2, 237.5 ksi	195	3.39	203	3.7	233	7.07
Test 3, Debond	311	3.15	326	4.7	333	3.41
Test 3, Flexure	311	3.15	326	4.8	334	3.41
Test 4.1 (250 ksi)	241	3.88	240	-0.4	253	4.63
Test 5, Manufacturer	221	3.00	244	10.2	274	4.63
Test 5, Experimental	221	3.00	240	8.8	267	4.59
Test 6, Manufacturer	269	3.39	278	3.5	293	3.99
Test 6, Experimental	269	3.39	273	1.4	289	3.94

The validation analyses also allow the determination of which of the alternative stress-strain curves are to be employed for the various retrofit measures, in the remainder of the present study. Regarding the strand-splice repair, a splice failure stress of 225 ksi is selected for an eight-strand splice, while a failure stress of 250 ksi is selected for a four-strand splice. For the retrofit using overlays of FRP and FRCM, the validation analyses are inconclusive. The fact that no significant damage is observed in the retrofitted tensile zones of the cross-sections precludes the reliable determination of which of the alternative stress-strain curves is to be used. Given that the analysis of the next chapter will be focused on prototype girders which fail in the tension zone and to provide conservative results, the stress-strain curves which give the minimum retrofit strength will be used for the FRP and FRCM. Thus, the stress-strain curve corresponding to crack-induced debonding of the FRP and the curve obtained from the FRCM material tests will be used for the remainder of this study.

CHAPTER 6 ANALYTICAL ASSESSMENT OF DAMAGED AND REPAIRED PROTOTYPE GIRDERS

6.1 Introduction

After the creation of analytical models for the six experimental test, the one undamaged girder and five repair methods, it is important to use the analytical modeling tools to evaluate the effectiveness of these repair methods. The experimental data was not comparable due to different spans being tested and the incompleteness of tests in showing full failure. Analytical modeling is used to run tests on equivalent prototype girder test setups to make a direct comparison between repair methods. The direct comparison test chosen to be run is with AASHTO loading conditions and limit states. This is done because these girders were initially designed with AASHTO provisions, and any subsequent repairs would take into account these provisions. AASHTO Standard Specifications for Highway Bridges allows for the flexural design strength of each girder in a bridge to be determined with the addition of an effective width of the concrete deck (AASHTO 2010). This effective width of concrete deck accounts for the composite deck action that occurs in the actual bridge.

Analytical modeling is done using the nonlinear beam models. Given that VDOT and practitioners use more simplified models to find the moment-curvature response of the girder sections, it is prudent to use nonlinear beam modeling which employs the sectional modeling approach. In this way, the results of these analyses are comparable to those that can be calculated using simplified AASHTO modeling procedures.

6.2 Prototype Girders

As a simplification, the girders are designed with effective width and loaded as interior girders. It is understood that impact damage is more likely to occur on exterior girders, but the inclusion of parapets complicates the analysis and the issues relevant in the present work (Harries, 2006). The main goal is to provide repair designs and model the repaired girder in order to verify the strength of the repair. Therefore, all girders modeled are considered to be interior and exclude parapets that add biaxial bending. Also, in the bridge blueprints there exists sufficient overhang on the exterior girders to model the bridge with the same effective deck as interior girders (Jones, 2015).

From the provisions in AASHTO Standard Specifications for Highway Bridges, Article 8.10.1 (AASHTO 2010) the effective width of the deck was found to be 88 inches, corresponding to the center to center distance between adjacent bridge girders. The cross-section of the prototype girder with the full effective bridge deck is shown in Figure 6.1.

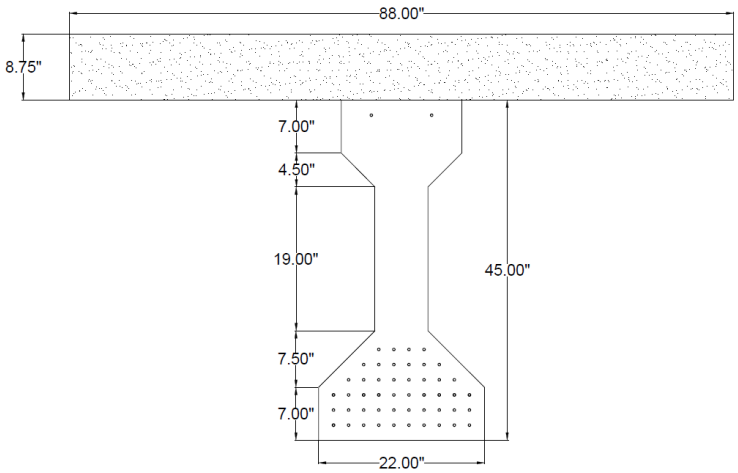

Figure 6.1: Prototype Girder Cross Section with Effective Bridge Deck

Two different limit states are used to verify the effectiveness of the repairs: strength and serviceability. To serve its purpose, a structure must be serviceable under ordinary use and must be safe against collapse (Nilson, 1987). The strength of the structure must be adequate enough to resist overloading should the loads be increased past regular service loads. Considerations for strength are found in Section 5.7 of AASHTO LRFD (AASHTO, 2010). The design load from Strength I is checked against the nominal capacity found through the analysis. Serviceability requires that deflections be suitability small, crack widths be kept within acceptable limits, and vibrations be minimized. In addition, most specifications impose limitations on the stresses in the concrete and steel. Considerations for serviceability are found in Article 5.9. Dead and live loads are applied with the Service I and Service III load factors. Compressive and tensile stresses in concrete and tensile stresses in the strands are checked for adequacy. In addition, the concrete section was checked to see if it remains un-cracked.

Bridge load calculations are completed according to AASHTO LRFD (AASHTO 2010) specifications and are compiled in Table 6.1. Calculations are detailed in Appendix A. Dead loads considered are the self-weight of the deck, self-weight of the girder, wearing surface, parapets, deck forms, and miscellaneous loads. Live loads are calculated based on a lane load and the load of the more critical HS-25 vehicle and the design Tandem vehicle. Since this specific bridge was originally built around 1960, it was originally designed for a lower HS-20 vehicle loading according to the 1960 AASHO Specifications. The total loads for the HS-20, HS-25, and Tandem trucks, including dead load, are shown in Table 6.1. From calculations it is determined that the HS-25 is more critical to represent the conditions for modern loading. Load factors are calculated from the provisions in Article 3.4. The load factors considered are with three limit states: Strength I, Service I, and Service III.

Table 6.1: AASHTO Load Calculation Summary

	Loading	Moment	Strength I	Service I	Service III	Units
M_Deck	0.85 k/ft	356	446	356	356	k-ft
M_Girder	0.57 k/ft	240	300	240	240	k-ft
M_Parapets	0.25 k/ft	105	131	105	105	k-ft
M_Deckforms	0.09 k/ft	38	47	38	38	k-ft
M_Miscellaneous	0.015 k/ft	6	8	6	6	k-ft
M_WearingSurface	0.082 k/ft	34	52	34	34	k-ft
M_Lane	0.64 k/ft	269	467	267	213	k-ft
M_HS20	HS20	764	1760	1010	805	k-ft
M_HS25	HS25	955	2200	1260	1010	k-ft
M_TANDEM	TANDEM	675	1560	890	712	k-ft
		HS20 (1960)	3210	2050	1800	k-ft
		HS25 (2010)	3650	2310	2000	k-ft
		TANDEM (2010)	3010	1940	1710	k-ft

The prototype analyses are modeled after the considerations of the bridge plans and the test setup used for the full girder test in Test 2. The prototype girder analysis is a 58 ft simple span that was damaged 4 ft on either side of the midpoint. Damage is completed at the mid-span because typical impact damage from over-height vehicles occurs around the mid-span of a girder, at which a truck is likely to hit. The length of damage on the prototype girder is 8 ft based on data from the YRC Freight Company indicating the average width of a semi-trailer as approximately 8 ft (YRC Worldwide, 2015).

Two different sets of analyses are conducted on the girders. The first set of analyses is completed to check strength limits. The Strength Analysis setup is shown in Figure 6.2. The load is applied as two point loads placed in the mid-span to keep the repaired section within a constant moment region. Thus, full flexural failure is initiated in the repaired region, showing the strength of the repair. The girder strength is then compared to the Strength I load

combinations for the HS-20 and HS-25 truck loadings, as well as used as direct comparison of repair strength.

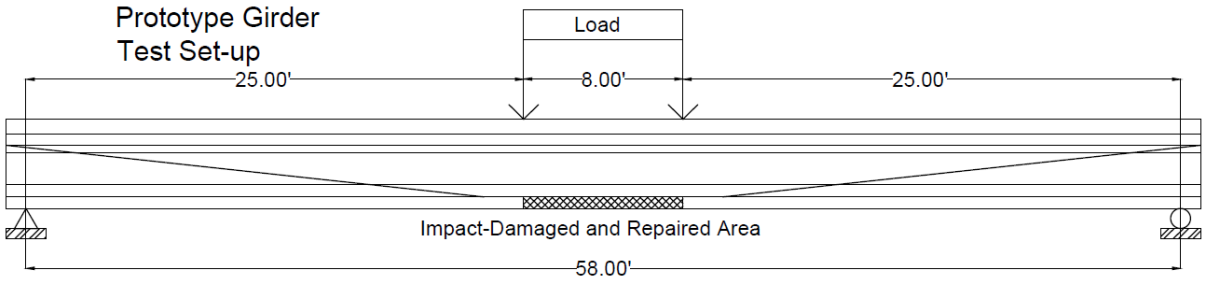

Figure 6.2: Prototype Girder Strength Analysis Setup

The second set of analyses is completed to check the serviceability limit states. During these service analyses, loading with Service I load combination is applied to check the compressive stresses in the concrete and tensile stresses in the steel strands. Service III load combination is applied to the check the tensile stresses in the concrete. Figure 6.3 shows the setup of this Service Analysis, with HS-20 truck loading, representing 1960 design standards. Additionally, the analysis is set up with HS-25 truck loading, representing 2010 design standards.

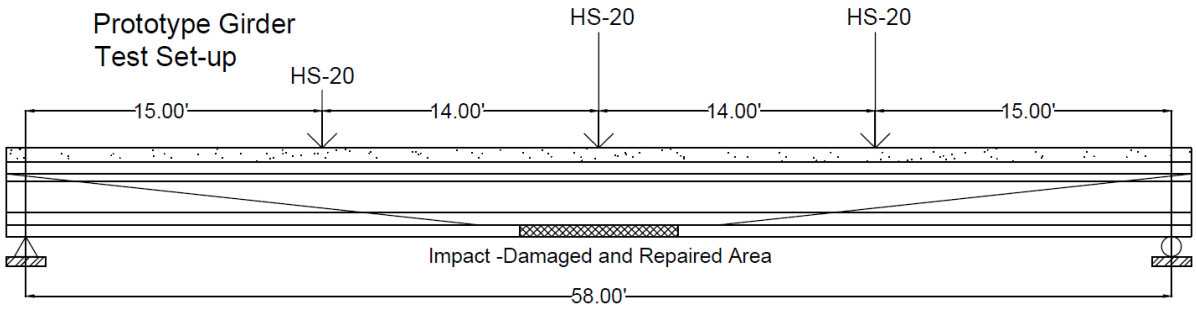

Figure 6.3: Prototype Girder Service Analysis Setup with HS-20 Truck Loading

Given that the nonlinear beam models provided very good results for the girders tested, such models are employed in this chapter for the analysis of the prototype bridges.

6.3 Analysis of Prototype Girders using Nonlinear Beam Models

All five repair methods investigated in the experimental tests are modeled. The material strengths used for both the concrete and steel strands used were the experimentally tested values. For the splice repairs, it is assumed that the splices would have the same area as the other prestressing strands. For the FRP repairs, it is assumed that the FRP fibers would be 0.16 in thick (two layers), and span the entire 22 in of the bottom flange. For the FRCM repairs, it is assumed that the FRCM fibers would be 0.007 in thick (four layers), and be located on the entire bulb of the bottom flange.

6.3.1 Analysis for AASHTO Strength Limit States

For the Prototype Girder Strength Analysis nonlinear beam model, a displacement controlled analysis in OpenSees is run. The displacement was controlled at the load points and the corresponding force required to displace these nodes was measured. The moment and curvature of elements in the constant moment region is recorded during the analysis. This leads to a moment-curvature plot, which shows the response of the beam to the recreated testing scenario. From the moment-curvature plot two points are of interest: first yielding and ultimate strength. The curvature at yielding, and the resultant moment to cause yielding, correspond to the point at which the first steel strand reaches the yield stress. Ultimate strength is important in finding repair capacity. The curvature at ultimate strength corresponds to the point at which the

first failure mode occurs. This can be either concrete crushing (compressive concrete reaching a strain of 0.003), full tensile failure (first steel strand reaching a strain of 0.05), strand splice rupture, FRP debonding, or FRCM debonding. The ratio of ultimate curvature to first yielding curvature, known as curvature ductility, is important in determining the ductility of each repair method. An ideal repair method would have good ductility to give warning of imminent girder failure. The results of these analyses are summarized in Table 6.2.

The first set of analyses run is the baseline models: the undamaged model, the four strand damaged model, and the eight strand damaged girder. The moment-curvature response for these girders is shown in Figure 6.4. The failure method for all three analyses is a full flexural failure, with the steel reinforcing strands rupturing at an ultimate strain of 0.05. Ideally, the repairs will restore the full undamaged capacity. If not this is not achieved, it would have to be verified that the repair method has enough strength capacity to satisfy the Strength I limit state. Table 6.3 compares all of the repairs, using the undamaged condition as a baseline to compare capacity and ductility. From observation, by damaging the strands a significant loss in strength is seen (91.2% capacity with four strands damaged and 82.1% capacity with eight strands damaged). Though ductility does not suffer, with the four strands damaged model reaching 98.9% ductility and the eight strands damaged model reaching 95.1% ductility.

The analyses are repeated with the five repair methods experimentally tested. The first is the four strand splice repair tested in Test 4. The moment-curvature response is shown in Figure 6.5a, comparing it to the undamaged condition and the fully damaged four strand condition. The failure method in the analysis is spliced strand rupture at a failure stress of 250 ksi, the full splice strength (f_{pu}).. From observation, the repair restores 92.9% capacity and 37.4% ductility. After failure, the curve returned to the curve of the fully damaged condition, as expected.

The second repair analyzed is the eight strand splice repair tested in Test 2. The moment-curvature response is shown in Figure 6.5b, comparing it to the undamaged condition and the fully damaged eight strand condition. The failure method in the analysis is spliced strand rupture at a failure stress of 225 ksi, (0.90 f_{pu}). The premature splice strength failure model observed in testing. From observation, the repair restores 85.3% capacity and 11.5% ductility. The four strand FRP repair tested in Test 3 is the third repair method analyzed. The moment-curvature response is shown in Figure 6.6, comparing it to the undamaged condition and the fully damaged four strand condition. The failure method in the analysis is intermediate crack-induced debonding failure of the FRP at a strain of 0.005173. From observation, the repair restores 100.6% capacity and 11.6% ductility.

The fourth repair analyzed is the four strand FRCM repair tested in Test 4. The moment-curvature response is shown in Figure 6.7a, comparing it to the undamaged condition and the fully damaged four strand condition. The failure method in the analysis is FRCM debonding at a strain of 0.012. From observation, the repair restores 90.2% capacity and 26.4% ductility. The final repair analyzed is the only combined repair method; the four strand FRCM and strand splice repair tested in Test 6. The moment-curvature response is shown in Figure 6.7b comparing it to the undamaged condition and the fully damaged four strand condition. The failure method in the analysis is also FRCM debonding at a strain of 0.012. From observation, the repair restores 98.1% capacity and 26.4% ductility.

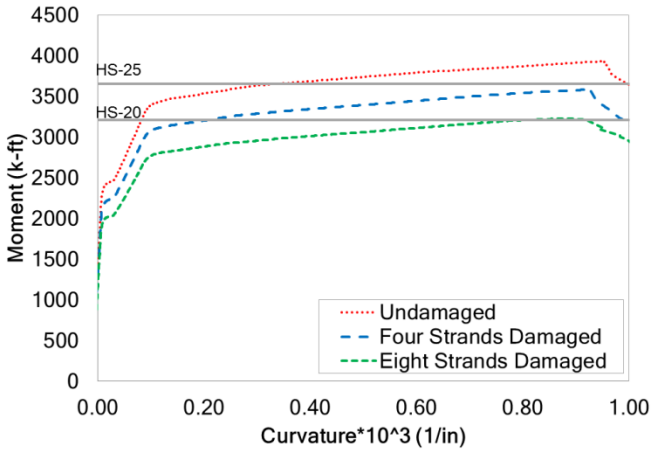

Figure 6.4: Moment-Curvature Response of Prototype Undamaged and Damaged Girder

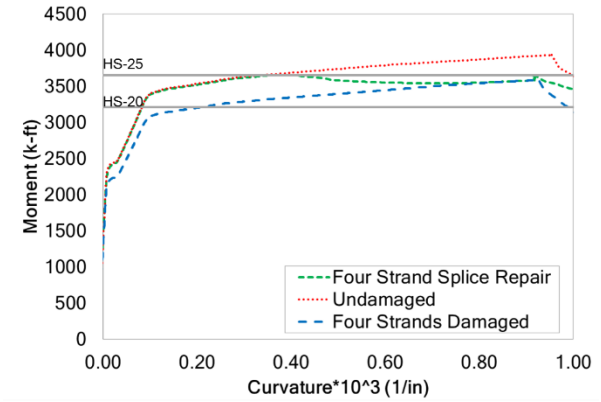

a) Splice Repair on 4 Strands

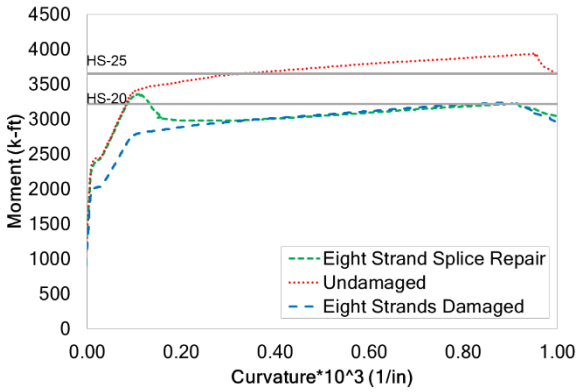

b) Splice Repair on 8 Strands

Figure 6.5: Moment-Curvature Response of Prototype Girder Investigating the Effect of Strand Splice Repair

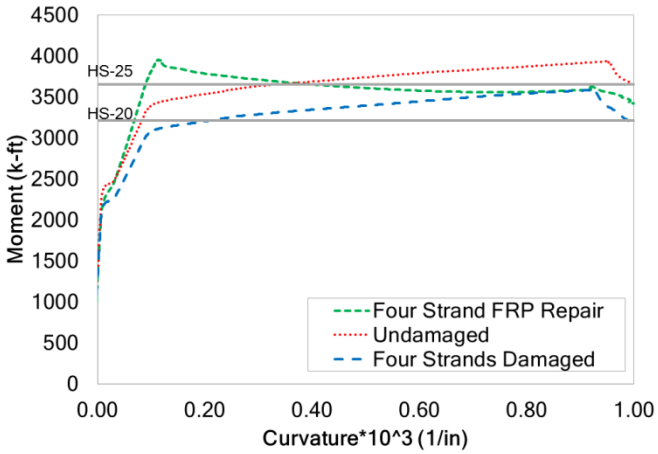

Figure 6.6: Moment-Curvature Response of Prototype Girder Investigating the Effect of an FRP overlay on a girder with 4 strands damaged

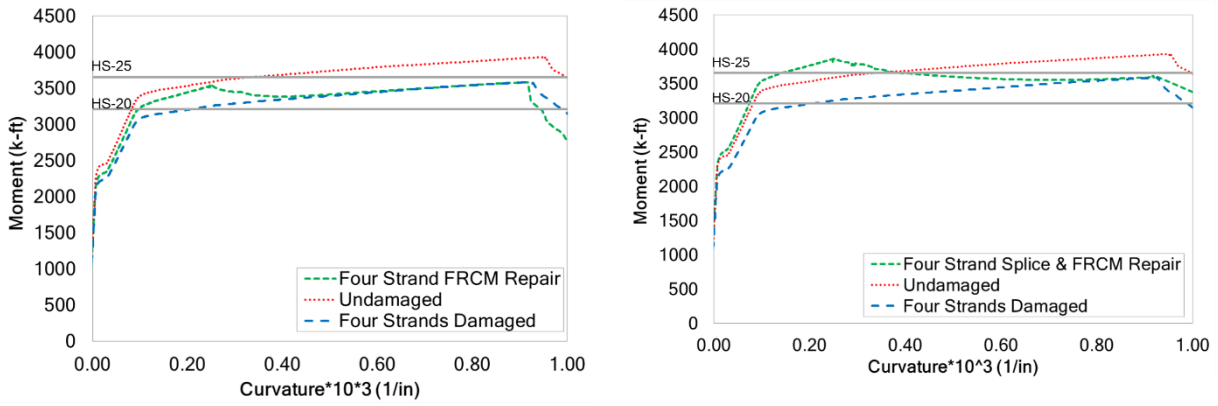

a) FRCM Overlay and 4 Strands Damaged **b) FRCM Overlay and Splice Repair on 4 Strands**

Figure 6.7: Moment-Curvature Response of Prototype Girder Investigating the Effect of a Repair Using FRCM Overlays.

Table 6.2: Prototype Girder Strength Analysis Nonlinear Beam Model Summary

Case	Moment at First Yielding (k-ft)	Curvature at First Yielding (1/in)	Moment at Ultimate (k-ft)	Curvature at Ultimate (1/in)	Curvature Ductility
Undamaged	3300	0.000088	3930	0.00095	10.73
4 Strands Damaged	2990	0.000087	3580	0.00093	10.61
8 Strands Damaged	2680	0.000087	3230	0.00088	10.21
4 Strands Spliced	3290	0.000088	3650	0.00035	4.01
8 Strands Spliced	3240	0.000088	3360	0.00011	1.23
4 Strands FRP	3630	0.000090	3960	0.00011	1.25
4 Strands FRCM	3130	0.000087	3550	0.00025	2.83
4 Strands Spliced & FRCM	3430	0.000088	3860	0.00025	2.83

Table 6.3: Prototype Girder Strength Analysis Nonlinear Beam Model Comparison

Case	Percentage of Undamaged Capacity (%)	Percentage of Undamaged Ductility (%)	HS-20 Moment Demand (k-ft)	Percentage of HS-20 Demand Met (%)	HS-25 Moment Demand (k-ft)	Percentage of HS-25 Demand Met (%)
Undamaged	100	100	3210	122	3650	108
4 Strands Damaged	91.2	98.9	3210	112	3650	98.1
8 Strands Damaged	82.1	95.1	3210	101	3650	88.4
4 Strands Spliced	92.9	37.4	3210	114	3650	100
8 Strands Spliced	85.3	11.5	3210	105	3650	91.9
4 Strands FRP	101	11.6	3210	123	3650	108
4 Strands FRCM	90.2	26.4	3210	110	3650	97.1
4 Strands Spliced & FRCM	98.1	26.4	3210	120	3650	106

6.3.2 Analysis for AASHTO Service Limit States

For the Prototype Girder Service Test nonlinear beam model, a static analysis in OpenSees is run. The distributed loads due to dead and live load, as well as the varying truck loads are applied statically. Stresses in the concrete and steel fibers in the midpsan, at which point moment was maximum, are recorded. During these service tests, loading with Service I load combination is applied to check the compressive stresses in the concrete and tensile stresses in the steel strands. Service III load combination is applied to the check the tensile stresses in the concrete. These stresses are checked against AASHTO stress provisions (AASHTO 2010). Compressive stress in concrete is limited to $0.45 * f_c'$. Tensile stress in concrete is limited to $0.19 * \sqrt{f_c'}$. Tensile stress in prestressing strands is limited to $0.80 * f_{pu}$. The section also had to be verified to be un-cracked.

The analysis is run for HS-20 and HS-25 truck loading. These two loadings represent the design truck loadings for 1960 and 2010 respectively. The HS-20 analysis reveals that all repairs, even the fully damaged cases, are satisfied. The HS-25 analysis, summarized in Table 6.4, reveals that all repairs satisfy the serviceability requirements.

Table 6.4: Prototype Girder Service Analysis Nonlinear Beam Model Comparison for HS-25 Truck Loading

Case	Compressive Stress at Top Deck Concrete (ksi)	Service I Limit State (ksi)	Tensile Stress at Bottom Girder Concrete (ksi)	Service III Limit State (ksi)	Tensile Stress at Bottom Girder Srand (ksi)	Service III Limit State (ksi)
Undamaged	-0.81	-2.71	0.24	0.49	144	200
4 Strands Damaged	-1.03	-2.71	0.40	0.49	159	200
8 Strands Damaged	-1.43	-2.71	0.32	0.49	198	200
4 Strands Spliced	-0.83	-2.71	0.27	0.49	145	200
8 Strands Spliced	-0.85	-2.71	0.29	0.49	146	200
4 Strands FRP	-0.92	-2.71	0.40	0.49	151	200
4 Strands FRCM	-0.89	-2.71	0.37	0.49	149	200
4 Strands Spliced & FRCM	-0.80	-2.71	0.19	0.49	144	200

6.4 Discussion

The repair that performed the best in terms of strength capacity restored was the four strand FRP repair, tested experimentally in Test 3, with 101%, though it provided a mere 11.6% of the ductility of the undamaged condition. The repair that restored the most ductility was the four strand splice repair, tested experimentally in Test 4, with 37.4% ductility restored, though it provided only 92.9% capacity. The improvement was minor compared to the 91.2% capacity of the four strand fully damaged condition. The repair with the best combination of capacity and ductility restored was the four strand combined FRCM and splice repair, tested experimentally in Test 6. This repair restored 98.1% capacity and 26.4% ductility.

Table 6.4 compares the capacity of the repair methods to the different Strength I service limit states. From observation, all repair methods, even the fully damaged cases, satisfy the HS-20 design loading used in 1960. Only the three previously mentioned repair methods (four

strand splice, four strand FRP, and four strand FRCM and splice) satisfy the HS-25 design loading used in 2010.

The only model that did not satisfy the serviceability requirements was the eight strand fully damaged model, which showed cracking in the concrete in the tensile zone. Though it can be seen that the stress in the tensile concrete was less than the service limit state, this was because the concrete had reached peak tensile strength and had effectively cracked.

CHAPTER 7 CONCLUSIONS AND RECOMMENDATIONS

7.1 Summary

This thesis covers the creation of analytical models to verify the results of six flexural tests conducted on damaged and repaired AASHTO Type III bridge girders. Test 1 was on an undamaged girder section. Test 2 was on a girder with eight severed strands that were re-tensioned with Grabb-it strand splices (Prestress Supply Incorporated, 2010). Test 3 was on a girder with four severed strands that was repaired with V-wrap 400 FRP (Structural Group Incorporated, 2015). Test 4 was on a girder with four severed strands that were re-tensioned with Grabb-it strand splices. Test 5 was on a girder with four severed strands that were repaired with Ruredil X-Mesh Gold FRCM (Ruredil X Mesh Gold, 2012). Test 6 was on a girder with four severed strands that were re-tensioned with Grabb-it strand splices and repaired with Ruredil X-Mesh Gold FRCM. The thesis also discusses the extension of these repair methods to prototype girder models with an effective width of concrete deck to serve as comparison for the effectiveness of the repair. These prototype girder models were representative of AASHTO design standards for girders and AASHTO loading was applied to the models (AASHTO, 2010).

7.2 Conclusions

Two different analytical modeling techniques were chosen for this investigation. Nonlinear beam modeling was pursued using the analysis program OpenSees (Mazzoni, et al , 2006). Three-dimensional, continuum-based, finite element modeling was conducted using the commercial program LS-DYNA (Hallquist, 2007). The nonlinear beam models used beam elements with a fiber-section discretization of the girder section. This was seen as a simplified

modeling technique and is computationally inexpensive. The finite element models used three-dimensional solid elements. There are many aspects that were seen to be more accurately modeled using continuum-based FE. The advantages were the elements were able to be further discretized, and a more accurate representation of three-dimensional behavior due to unsymmetrical cross-sections, support conditions, spreader beam loading, and harped strands. The disadvantages were the high computational cost and the difficulty to create the model.

The use of two modeling techniques was beneficial to the present study, in large part due to the good accuracy of both modeling techniques. A synergistic use of the simpler beam models and the more refined finite element (FE) models was able to reduce the required number of FE analyses. In other words, the simpler beam models were used to calibrate a large set of variables, and once refined by the beam models, the more complex FE models could be used to further verify these calibrations on a smaller set of variables.

From observation, the modeling technique that was more accurate to experimental data was the nonlinear beam modeling. For the validated models of the six experimental tests, the nonlinear beam models had an average error of 1.9%, compared to the average error in the continuum-based FE models of 2.8%. Also, the continuum-based FE models tended to over predict the ultimate strength of the girder. The nonlinear beam modeling technique was more conservative, more accurate, and more computationally inexpensive. The very good accuracy of the beam models indicates that they can be used alone, at least at a preliminary stage, for the performance assessment of damaged and repaired girders. Of course, the analyst must always be aware that a beam model cannot explicitly account for potentially crucial effects such as diagonal cracking.

By examining the accuracy of the nonlinear beam models to the experimental tests, the models can be further judged on their ability to predict the capacity of the girder. Only three of the tests reached full flexural failure; Test 2 with eight strands spliced, Test 4 with four strands spliced, and Test 6 with four strands spliced and repaired with FRCM. Test 2 failed at a load of 195 kips, while the model predicted failure at 198 kips, an over prediction of 1.5%. Test 4 failed at a load of 265 kips, while the model predicted 270 kips, an over prediction of 1.9%. Test 6 failed at a load of 269 kips, while the model predicted 276 kips, an over prediction of 2.6%. From observation, these models are accurate, but a bit un-conservative. It is recommended that if these models are used for prediction, this un-conservative nature is taken into account.

The predefined configuration of the experimental specimens did not include the entire deck region which will be effective as a compressive zone in the girder section. For this reason, the vast majority of the repaired specimens incurred strength degradation due to crushing at the compressive zone of the section. Additional experimental tests are recommended on girder configurations which will lead to severe damage in the tension zone of the damaged cross-section, allowing an even more reliable calibration of constitutive models for the retrofit measures.

Considering the repair methods to be accurately modeling using the nonlinear beam modeling, the models were then extended to prototype girder models with an effective width of concrete deck to serve as comparison for the effectiveness of the repair. Of the five repair methods investigated, four of the repairs were performed with a single repair technique and one was performed with a combination of repair techniques. The combined four strand splice and FRCM repair restored 98.1% of the undamaged capacity and 26.4% of the undamaged ductility. The four strand splice repair alone restores 92.9% capacity and 37.4% ductility. The four strand

damaged FRCM repair alone restores 90.2% capacity and 26.4% ductility. From observation, combining repair methods is seen to result in an additive effect on strength, but have the curvature at failure of the less ductile repair method. In this case, the less ductile repair method was FRCM. This effect of combining repairs on ductility should be considered when designing repair methods.

There is a discrepancy between the splice models depending on the amount of strands spliced. With more strands spliced, more stress is concentrated in the splice chuck, and the splice rupture was not purely tensile, but a combination of shear and tension. A splice failure stress of 225 ksi is selected for an eight-strand splice, while a failure stress of 250 ksi is selected for a four-strand splice. For the purposes of design of a strand splice repair, it is recommended to use the 225 ksi (0.9 f_{pu}) failure stress material model for splices. This model is more conservative and accounts for the premature splice rupture that was seen in Test 2. Two different damage levels were investigated for strand splices. The only eight strand repair investigated in the present study, eight strands spliced, restored 85.3% of the undamaged capacity, and meets 91.9% of the HS-25 truck demand. It is not recommended to use strand splice repair on this level of damage because the repair will not provide restore enough strength necessary strength to the girder.

Concerning repair using FRP overlays, this repair method was seen to restore the least ductility to the girder section. The FRP repair on four damaged strands restored 100.6% of the undamaged capacity, though only 11.6% of the ductility. This is due to the intermediate crack-induced debonding failure mode. It is important to design for this failure mode because it can occur prematurely and cause the debonded FRP overlay to detach.

For the FRCM repair, the experimentally determined material model was determined to be more accurate and conservative. Though, determining this bilinear curve requires experimental testing, which may not be available to a designer. If a designer is unable to determine the experimental properties of the FRCM, it is recommended that they use the manufacturer's elastic model. This model is slightly less conservative, but provides an appropriate estimate of strength restored.

In general, for the design of impact-damaged prestressed concrete girder repairs, it is recommended that the design be calibrated to current design truck loading standards. These current design trucks are more representative of present day traffic load, and will result in a more conservative design.

The validated simulation tools enable the extensive parametric performance assessment for damaged and repaired prototype bridge beams and systems. The beam-based models can even be used in practice, for the assessment of the impact of collision-induced damage and the selection of repair techniques (if necessary) for actual bridge systems.

7.3 Recommendations

Recommendations for further research into the repair methods of impact damaged prestressed bridge girders include:

1. Extend analytical modeling to repairs that were unable to be tested experimentally. Suggestions include combined splice and FRP and repairs with a damage level of eight strands.

2. Extend analytical modeling to real exterior girder conditions. This would account for the biaxial bending caused by the presence of the parapets.
3. Extend analytical modeling to a full bridge model, with all four girders. In this proposed model, only the one exterior girder would receive the impact damage.
4. Investigate the effects of repair techniques on different girder cross sections, not just the AASHTO Type III girder tested.

REFERENCES

AASHTO. (2010). *AASHTO LRFD Bridge Design Specifications* . Washington, DC: American Association of State Highway and Transportation Officials.

ACI . (2008). *Guide for the Design and Construction of Externally Bonded FRP Systems for Strengthening Concrete Structures.* ACI Committee 440.

ACI. (2013). *Guide to Design and Construction of Extenally Bonded Fabric-Reinforced Cementitious Matrix (FRCM) Systems for Repair and Strengthing Concrete and Masonry Structures.* Farmington Hills: American Concrete Institute.

Agrawal, A. K., Xu, X., & Chen, Z. (2013, January 15). *Strikes on Low Clearance Bridges by Over-Height Trucks in New York State.* Retrieved December 05, 2014, from United States Department of Transportation: http://www.rita.dot.gov/utc/publications/spotlight/2013_01/html/spotlight_0113.html

Aktan, A. E., Culmo, M. P., Frangopol, D. M., French, C. W., Rabbat, B. G., Sanders, D. H., . . . Woods, S. W. (1994). *Concrete Bridges.* Washington D.C.: Transportation Research Board: Committee on Concrete Bridges. Retrieved December 8, 2014

Brice, R. (2013). *Precast-Prestressed Concrete Girders Damaged by Over-Height Load Impacts.* Olympia: Washington State Department of Transportation. Retrieved December 13, 2014

Broadhouse, B. (1995). The Winfrith concrete model is LS-DYNA3D. *Report: SPD/D*, 363.

Chang, F.-K., & Chang, K.-Y. (1987). A progressive damage model for laminated composites containing stress concentrations. *Journal of Composite Materials 219*, 834-855.

ElSaftey, A., Graeff, M. K., & Fallaha, S. (2014, March). Behavior of Laterally Damaged Prestressed Concrete Bridge Girders Repaired with CFRP Laminates Under Static and

Fatigue Loading. *International Journal of Concrete Structures and Materials, VIII*(1), 43-59. Retrieved December 7, 2014

FHWA-HRT-05-062. (2007). *Users Manual for LS-DYNA Concrete Material Model 159.* McLean, VA: US Department of Transportation Federal Highway Administration.

Fu, C. C., Burhouse, J. R., & Chang, G.-L. (2003). *Study of Overheight Vehicle Collisions with Highway Bridges.* University of Maryland, Department of Civil & Environmental Engineering. College Park: Transportation Research Board of the National Academies. Retrieved December 7, 2014

Hallquist, J. O. (2007). *LS-DYNA keyword user's manual.* Livermore Software Technology Corporation.

Harries, K. (2006). *Full-scale Testing Program on De-commissioned Girders from the Lake View Drive Bridge.* Pittsburgh, PA: University of Pittsburgh.

Harries, K. A., Kasan, J., Miller, R., & Brinkman, R. (2012). *Updated Research for Collision Damage and Repair of Prestressed Concrete Beams.* NCHRP Project 20-07, Task 307, University of Pittsburgh, Department of Civil Engineering, Pittsburgh. Retrieved December 10, 2014

Hisham, M., & Mohd, Y. (1994). *Nonlinear Analysis of Prestressed Concrete Structures under Monotonic and Cycling Loads.* PhD dissertation, University of California, Berkeley.

International Code Council Evaluation Service. (2014). *ICC-ES Evaluation Report - V-Wrap Fiber-Reinforced Polymer Composite System.* Hanover: Structural Technologies, LLC.

Jones, M. (2015). *Repair Techniques of Impact Damaged Prestressed Bridge Girders Using Strand Splice and Fiber Reinforced Cementitious Matrix.* Virginia Polytechnic Institute

and State University, Department of Civil and Environmental Engineering. Blacksburg: Virginia Center for Transportation Innovation and Research.

Kasan, J. L. (2009). *Structural Repair of Prestressed Concrete Bridge Girders.* University of Pittsburgh, Department of Civil and Environmental Engineering . Pittsburgh: Swanson School of Engineering. Retrieved December 7, 2014

Kasan, J. L., Harries , K. A., Miller, R., & Brinkman, R. J. (2014). Repair of Prestressed-Concrete Girders Combining Internal Strand Splicing and Externally Bonded CFRP Techniques. *Journal of Bridge Engineering*, 200-209.

Kim, Y., Green, M., & Fallis, G. (2008). Repair of Bridge Girder Damaged by Impact Loads with Prestressed CFRP Sheets. *Journal of Bridge Engineering ASCE January/Februrary*, 15-23.

Mazzoni, S., McKenna , F., Scott, M., & Fenves , G. (2006). *OpenSees command language manual.* Berkeley, CA: Pacific Earthquake Engineering Research (PEER) Center.

McGuire, W., & Gallagher, R. (2015). *Matrix Structural Analysis.* CreateSpace Independent Publishing Platform.

Nilson, A. H. (1987). *Design of Prestressed Concrete* (2nd ed.). New York, New York, United States: John Wiley & Sons.

Ottosen, N. (1977). A failure criterion for concrete. *Journal of Engineering Mechanics 103*, 527-535.

Pino, V., & Nanni, A. (2015). *Repair of Damaged Prestressed Concrete Girder with Fabric Reinforced Cementitious Matrix and Fiber Reinforced Polymer Composites.* University of Miami, College of Engineering, Gables.

Prestress Supply Incorporated. (2010). *Grabb-It Cable Splice*. Retrieved December 12, 2014, from Prestress Supply: http://www.prestresssupply.com/Products/StrandRepair/GRABBITCableSplice.aspx

Prestress Supply Incorporated. (2010). *Grabb-It Torque Charts*. Retrieved December 12, 2014, from Prestress Supply: http://www.prestresssupply.com/Products/StrandRepair/GRABBITCableSplice/GRABBITCharts.aspx

Ruredil X Mesh Gold. (2012). *PBO Mesh in Stabalized Inorganic Matrix for Flexural and Shear Strength Reinforcment of Concrete.* Milan, Italy: Ruredil SPA.

Sen, R., Liby, L., & Mullins, G. (2001). Strengthening Steel Bridge Sections Using CFRP laminates. *Composites: Part B 32*, 309-322.

Shapiro, K. A. (2007). *Finite-Element Modeling of a Damaged Prestressed Concrete Bridge* . Auburn, AL: Auburn University.

Structural Group Incorporated. (2015). *Structural Technologies*. Retrieved May 1, 2015, from Structural Technologies, A Structural Group Company: http://www.structuraltechnologies.com

Teng, J., Chen, J., Smith, S., & Lam, L. (2002). *FRP Strengthened RC Structures.* West Sussex, England: John Wiley & Sons, Ltd.

Tumialan, G. (2014). FRCM Systems. *Structures Magazine*.

Wipf, T. J., Klaiber, F. W., Rhodes, J. D., & Kempers, B. J. (2004a). *Effective Structural Concrete Repair*. Iowa State University of Science and Technology, Department of Civil, Construction and Environmental Engineering. Ames: Iowa Department of Transpotation.

Wipf, T. J., Klaiber, F. W., Rhodes, J. D., & Kempers, B. J. (2004b). *Effective Structural Concrete Repair: Repair of Impact Damaged Prestressed Concrete Beams with Carbon Fiber Reinforced Polymer (CFRP).* Iowa State University, Department of Civil, Construction, and Environmental Engineering. Ames: Iowa Department of Transportation. Retrieved December 12, 2014

YRC Worldwide. (2015). *Trailer Dimensions*. (WordPress.com) Retrieved February 8, 2015, from YRC Freight: http://yrc.com/trailer-dimensions/

Zou, H., & Luo, X. (2012). Finite Element Analysis of the Corrosion Prestressed Concrete Beam. *Applied Mechanics and Materials Vols. 204-208*, 3040-3043.

APPENDICES

APPENDIX A: AASHTO Load Calculations

Load factors and combinations were found using AASHTO LRFD Bridge Design Specification Table 3.4.1-1 and 3.4.1-2. Dead loads were calculated using material unit weights found in AASHTO Table 3.5.1-1.

Table A.1: AASHTO Table 3.4.1-1 – Load Combinations and Load Factors (AASHTO, 2010) www.transportation.org

Load Combination Limit State	*DC DD DW EH EV ES EL PS CR SH*	*LL IM CE BR PL LS*	*WA*	*WS*	*WL*	*FR*	*TU*	*TG*	*SE*	Use One of These at a Time				
										EQ	*BL*	*IC*	*CT*	*CV*
Strength I (unless noted)	γ_p	1.75	1.00	—	—	1.00	0.50/1.20	γ_{TG}	γ_{SE}	—	—	—	—	—
Strength II	γ_p	1.35	1.00	—	—	1.00	0.50/1.20	γ_{TG}	γ_{SE}	—	—	—	—	—
Strength III	γ_p	—	1.00	1.40	—	1.00	0.50/1.20	γ_{TG}	γ_{SE}	—	—	—	—	—
Strength IV	γ_p	—	1.00	—	—	1.00	0.50/1.20	—	—	—	—	—	—	—
Strength V	γ_p	1.35	1.00	0.40	1.0	1.00	0.50/1.20	γ_{TG}	γ_{SE}	—	—	—	—	—
Extreme Event I	γ_p	γEQ	1.00	—	—	1.00	—	—	—	1.00	—	—	—	—
Extreme Event II	γ_p	0.50	1.00	—	—	1.00	—	—	—	—	1.00	1.00	1.00	1.00
Service I	1.00	1.00	1.00	0.30	1.0	1.00	1.00/1.20	γ_{TG}	γ_{SE}	—	—	—	—	—
Service II	1.00	1.30	1.00	—	—	1.00	1.00/1.20	—	—	—	—	—	—	—
Service III	1.00	0.80	1.00	—	—	1.00	1.00/1.20	γ_{TG}	γ_{SE}	—	—	—	—	—
Service IV	1.00	—	1.00	0.70	—	1.00	1.00/1.20	—	1.0	—	—	—	—	—
Fatigue I— *LL, IM & CE* only	—	1.50	—	—	—	—	—	—	—	—	—	—	—	—
Fatigue II— *LL, IM & CE* only	—	0.75	—	—	—	—	—	—	—	—	—	—	—	—

Table A.2: AASHTO Table 3.4.1-2 – Load Factors for Permanent Loads, γ_p (AASHTO, 2010)

Type of Load, Foundation Type, and Method Used to Calculate Downdrag		Load Factor	
		Maximum	Minimum
DC: Component and Attachments		1.25	0.90
DC: Strength IV only		1.50	0.90
DD: Downdrag	Piles, α Tomlinson Method	1.4	0.25
	Piles, λ Method	1.05	0.30
	Drilled shafts, O'Neill and Reese (1999) Method	1.25	0.35
DW: Wearing Surfaces and Utilities		1.50	0.65
EH: Horizontal Earth Pressure			
• Active		1.50	0.90
• At-Rest		1.35	0.90
• *AEP* for anchored walls		1.35	N/A
EL: Locked-in Construction Stresses		1.00	1.00
EV: Vertical Earth Pressure			
• Overall Stability		1.00	N/A
• Retaining Walls and Abutments		1.35	1.00
• Rigid Buried Structure		1.30	0.90
• Rigid Frames		1.35	0.90
• Flexible Buried Structures			
o Metal Box Culverts and Structural Plate Culverts with Deep Corrugations		1.5	0.9
o Thermoplastic culverts		1.3	0.9
o All others		1.95	0.9
ES: Earth Surcharge		1.50	0.75

Table A.3: AASHTO Table 3.5.1-1 – Unit Weights (AASHTO, 2010)

Material		Unit Weight (kcf)
Aluminum Alloys		0.175
Bituminous Wearing Surfaces		0.140
Cast Iron		0.450
Cinder Filling		0.060
Compacted Sand, Silt, or Clay		0.120
Concrete	Lightweight	0.110
	Sand-Lightweight	0.120
	Normal Weight with $f'_c \leq 5.0$ ksi	0.145
	Normal Weight with $5.0 < f'_c \leq 15.0$ ksi	$0.140 + 0.001\, f'_c$
Loose Sand, Silt, or Gravel		0.100
Soft Clay		0.100
Rolled Gravel, Macadam, or Ballast		0.140
Steel		0.490
Stone Masonry		0.170
Wood	Hard	0.060
	Soft	0.050
Water	Fresh	0.0624
	Salt	0.0640
Item		Weight per Unit Length (klf)
Transit Rails, Ties, and Fastening per Track		0.200

Live Loads factors were calculated using the AASHTO Table 3.6.1.1.2-1 and Table 3.6.2.1-1. The HS-20 design Truck Load from Figure 3.6.1.2.2-1.

Table A.4: AASHTO Table 3.6.1.1.2-1 – Multiple Presence Factors, *m* (AASHTO, 2010)

Number of Loaded Lanes	Multiple Presence Factors, *m*
1	1.20
2	1.00
3	0.85
>3	0.65

Table A.5: AASHTO Table 3.6.2.1-1 – Dynamic Load Allowance, *IM* (AASHTO, 2010)

Component	IM
Deck Joints—All Limit States	75%
All Other Components:	
• Fatigue and Fracture Limit State	15%
• All Other Limit States	33%

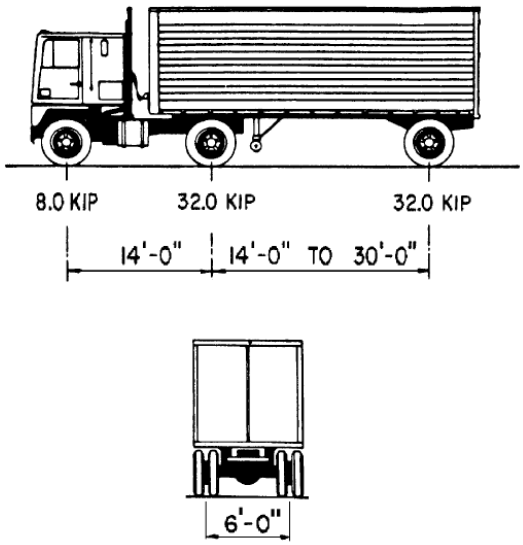

Figure A.1: AASHTO Figure 3.6.1.2.2-1 – Characteristics of the Design Truck (AASHTO, 2010)

AASHTO Equation C4.6.2.2.2.d-1 for live load flexural moment for exterior beams calculates the percentage of the design truck being applied to the exterior beam (AASHTO, 2010).

$$R = \frac{N_L}{N_b} + \frac{X_{ext} \sum_{N_L} e}{\sum_{N_b} x^2} \quad \text{(C4.6.2.2.2.d-1)}$$

Where:

$R =$ reaction on exterior beam in terms of lanes

$N_L =$ number of loaded lanes under consideration

$e =$ eccentricity of a design truck or a design lane load from the center of gravity of the pattern of girders (ft)

$x =$ horizontal distance from the center of gravity of the pattern of girders to each girder (ft)

$X_{ext} =$ horizontal distance from the center of gravity of the pattern of girders to the exterior girder (ft)

$N_b =$ number of beams or girders

APPENDIX B: Calculations for Externally Bonded FRP

To prevent intermediate crack-induced debonding failure mode, the effective strain in FRP reinforcement should be limited to the strain level at which debonding may occur, as defined in Equation 10-2 from the ACI 440 2R.08 document (ACI , 2008).

$$\varepsilon_{fd} = 0.083\sqrt{\frac{f'_c}{nE_f t_f}} \qquad (10\text{-}2)$$

Where:

ε_{fd}= debonding strain of externally bonded FRP reinforcement, in./in.

f'_c= specified compressive strength of concrete, psi

n = number of plies of FRP reinforcement

E_f = tensile modulus of elasticity of FRP, psi

t_f = nominal thickness of one ply of FRP reinforcement, in.

The FRP laminates should be anchored with transverse reinforcement to prevent the concrete cover layer from splitting. The area of the transverse clamping FRP U-wrap reinforcement can be determined in accordance with ACI Equation 13-1 (ACI , 2008).

$$A_{fanchor} = \frac{(A_{f*} f_{fu})longtidunal}{(E_{f*} \kappa_v * \varepsilon_{fu})anchor} \qquad (13\text{-}1)$$

Where the following definitions apply for the various terms:

$A_{fanchor}$ = area of transverse FRP U-wrap for anchorage of flexural FRP reinforcement

A_f = area of FRP external reinforcement, in.2

f_{fu}= design ultimate tensile strength of FRP, psi

κ_v = bond-dependent coefficient for shear

ε_{fu} = design rupture strain of FRP reinforcement, in./in.

The bond-reduction coefficient is a function of the concrete strength, the type of wrapping scheme used, and the stiffness of the laminate. The bond-reduction coefficient can be computed from ACI Equations 11-7 through 11-10 (ACI , 2008).

$$\kappa_v = \frac{k_1 * k_2 * L_e}{468 * \varepsilon_{fu}} \leq 0.75 \qquad (11\text{-}7)$$

$$L_e = \frac{2500}{(n * t_f * E_f)^{0.58}} \qquad (11\text{-}8)$$

$$k_1 = \left(\frac{f'_c}{4000}\right)^{2/3} \qquad (11\text{-}9)$$

$$k_2 = \frac{d_{fv} - L_e}{d_{fv}} \qquad (11\text{-}10)$$

The following definitions apply for the various factors appearing in Equations (11-7)-(11-10).

k_1 = modification factor applied to κv to account for concrete strength

k_2 = modification factor applied to κv to account for wrapping scheme

L_e = active bond length of FRP laminate, in.

d_{fv} = effective depth of FRP shear reinforcement, in.

l_{df} = development length of FRP system, in.